Computers and Fluids 198 (2020) 104385

Contents lists available at ScienceDirect

Computers and Fluids

journal homepage: www.elsevier.com/locate/compfluid

Incident shock wave and supersonic turbulent boundarylayer interactions near an expansion corner

Fulin Tong[a,b,c], Xinliang Li[a,d], Xianxu Yuan[b,c], Changping Yu[a,*]

[a] LHD, Institute of Mechanics, Chinese Academy of Sciences, 100190 Beijing, China
[b] State Key Laboratory of Aerodynamics, China Aerodynamics Research and Development Center, 621000 Mianyang, China
[c] Computational Aerodynamics Institute of China Aerodynamics Research and Development Center, 621000 Mianyang, China
[d] School of Engineering Science, University of Chinese Academy of Sciences, 100049 Beijing, China

ARTICLE INFO

Article history:
Received 19 April 2019
Revised 27 August 2019
Accepted 12 November 2019
Available online 13 November 2019

Keywords:
Shock wave
Turbulent boundary layer
Unsteadiness
Expansion corner

ABSTRACT

Direct numerical simulations of incident shock wave and supersonic turbulent boundary layer interactions near an expansion corner are performed at Mach number $M_\infty = 2.9$ and Reynolds number $Re_\infty = 5581$ to investigate the expansion effect on the characteristic features of this phenomenon. Four expansion angles, i.e. $\alpha = 0^0$ (flat-plate), 2^0, 5^0 and 10^0 are considered. The nominal impingement point of the oblique shock wave with a flow deflection angle of 12^0 is fixed at the onset of the expansion corner, and flow conditions are kept the same for all cases. The numerical results are in good agreement with previous experimental and numerical data. Various flow phenomena, including the flow separation, the post-shock turbulent boundary layer and the flow unsteadiness in the interaction region, have been systematically studied. Analysis of the instantaneous and mean flow fields indicates that the main effect of the expansion corner is to significantly decrease the size and three-dimensionality of the separation bubble. A modified scaling analysis is proposed for the expansion effect on the interaction length scale, and a satisfactory result is obtained. Distributions of the mean velocity, the Reynolds shear stress and the turbulent kinetic energy show that the post-shock turbulent boundary layer in the downstream region experiences a faster recovery to the equilibrium state as the expansion angle is increased. The flow unsteadiness is studied using spectral analysis and dynamic mode decomposition, and dynamically relevant modes associated with flow structures originated from the incoming turbulent boundary layer are clearly identified. At large expansion angle (α=10^0), the unsteadiness of the separated shock is dominated by medium frequencies motions, and no low frequency unsteadiness is observed. The present study confirms that the driving mechanism of the low frequency unsteadiness is strongly related to the separated shock and the detached shear layer.

1. Introduction

Shock wave and turbulent boundary layer interactions (SWTBLIs), owing to their ubiquitous occurrence and significant impact on the performance of high speed vehicles, have received extensive and sustained attention in the past decades. A large body of experimental and numerical studies on this subject has been performed and the advances are quite encouraging. Comprehensive summary on this subject can refer to the notable works reviewed by Clemens & Narayanaswamy [1] and Gaitonde [2]. When an incident oblique shock wave impinges at an expansion corner, the interactions are much more complicated as the flow structures can be significantly affected by the presence of the expansion corner. Due to a favorable pressure gradient induced by the expansion effect, SWTBLIs might be dramatically weakened with large expansion. Additionally, a turbulent boundary layer subjected to an expansion corner can undergo an acceleration and relaminarization process [3,4], unlike the strong amplification of turbulence intensity related to shock interactions. The combined effect of the shock cancellation and relaminarization on SWTBLIs is still not fully understood and the associated physical mechanisms need to be further investigated.

Numerous experimental investigations have been performed to study the behaviors of shock interactions near an expansion corner. Chew [5] experimentally investigated SWTBLIs in the presence of a 6^0 expansion corner at Mach numbers of 1.8 and 2.5. They

* Corresponding author.
E-mail address: cpyu@imech.ac.cn (C. Yu).

https://doi.org/10.1016/j.compfluid.2019.104385
0045-7930/

found that the interaction region could be strongly affected by the expansion corner only when the interaction occurred within three to four times of the boundary layer thicknesses upstream of the corner. Chung & Lu [6] carried out detailed experimental studies on the interactions between a Mach 8 turbulent boundary layer and an impinging shock near an expansion corner. The incident shock generated by an external sharp wedge impinged at three different locations, i.e. at the corner, ahead of the corner and after the corner. Their experiments showed that the upstream influence was significantly attenuated by the favorable pressure gradient induced by the expansion effect, especially when the shock impinged after the corner. However, due to small corner and wedge angles considered in their experiments, the boundary layers were all unseparated. White & Ault [7] carried out a similar experiment with stronger shock interactions and the separated flow occurred near the expansion corner. Collectively, measurements of the wall static pressure and heat transfer showed that as the separation region moved closer to the expansion corner, the separation was eventually suppressed. A small influence was also observed when the separation region was fully upstream of the corner. In recent years, Sathianarayanan & Verma [8] used surface oil-flow technique and the mean pressure measurement to investigate the incident shock and boundary layer interactions in the vicinity of an expansion corner and in the presence of sidewalls at $M_\infty = 3.9$. Their focus was laid on the effect of geometrical parameter variations on the three-dimensional nature of the separation, such as the wedge angle, the expansion angle and the impingement locations. Their experiments demonstrated that the three dimensionalities of the separated flow depended strongly on the wedge angle, rather than on the expansion angle, and the suppression of the separation was not fully completed even though the expansion angle was larger than the wedge angle.

In contrast to the relatively extensive experimental studies, only a very limited number of high-fidelity numerical studies, i.e. direct numerical simulation (DNS) and large eddy simulation (LES), on SWTBLIs near an expansion corner have been reported so far. Recently, Konopka et al. [9] performed LESs of a shock wave impinging on the supersonic boundary layer downstream of an expansion corner at $M_\infty = 1.76$, with focus on the turbulence statistics. They found that the Reynolds stress components were significantly amplified and a maximum amplification factor of 11 occurred for the wall-normal component. Analysis of the Reynolds stress anisotropy tensor also showed that the tendency towards the one-component limit at the expansion corner was reversed to approach the two-component limit for the near-wall turbulence due to shock interactions.

The main objective of this paper is to investigate the fundamental mechanisms associated with the SWTBLIs near an expansion corner using DNS. To the authors' knowledge, such DNS studies of SWTBLIs near an expansion corner are relatively rare in the literature. In present simulations, the nominal impingement location and the strength of the incident shock are fixed, and the expansion effect is highlighted with increasing the angle of the expansion corer. The inflow conditions and flow configurations are chosen to be similar to those used in the DNS of Priebe et al. [10] and in the experiments of Bookey *et al.* [11]. We focus particularly on the analysis of the separation region, turbulence statistics and unsteadiness in the interaction region to provide further insight about the complicated flow phenomena. The content of this paper is organized as follows. In Sec. II, details about the direct numerical simulations are introduced. The expansion effects on the separation region and the length scales are then presented in Sec. III. The characteristics of the post-shock turbulent boundary layer and the unsteadiness are discussed in Sections IV and V, respectively. In Sec. VI, conclusions are finally given.

2. Direct numerical simulations

2.1. Governing equations and numerical method

The compressible Navier–Stokes equations in conservative form can be written in curvilinear coordinates as follow,

$$\partial_t U + \partial_\xi (F - F_v) + \partial_\eta (G - G_v) + \partial_\zeta (H - H_v) = 0, \tag{1}$$

here, $U = J^{-1}(\rho, \rho u, \rho v, \rho w, \rho E)$ denotes the conservative vector flux, with ρ the density, (u, v, w) velocity components in three directions, and ρE the total energy. J^{-1} is the Jacobian matrix transforming Cartesian coordinates into curvilinear coordinates. F and F_v are inviscid and viscous fluxes in the direction $\boldsymbol{\xi}$, which can be expanded as

$$F = J^{-1}\begin{bmatrix} \rho\tilde{U} \\ \rho u\tilde{U} + \xi_x P \\ \rho v\tilde{U} + \xi_y P \\ \rho w\tilde{U} + \xi_z P \\ (\rho E + P)\tilde{U} \end{bmatrix} F_v = J^{-1}\begin{bmatrix} 0 \\ \xi_x\sigma_{11} + \xi_y\sigma_{21} + \xi_z\sigma_{31} \\ \xi_x\sigma_{12} + \xi_y\sigma_{22} + \xi_z\sigma_{32} \\ \xi_x\sigma_{13} + \xi_y\sigma_{23} + \xi_z\sigma_{33} \\ \boldsymbol{\xi_x} S_1 + \xi_y S_2 + \xi_z S_3 \end{bmatrix} \tag{2}$$

Where,

$$\tilde{U} = u\xi_x + v\xi_y + w\xi_z$$

$$S_1 = u\sigma_{11} + v\sigma_{21} + w\sigma_{31} - q_1$$

$$S_2 = u\sigma_{12} + v\sigma_{22} + w\sigma_{32} - q_2$$

$$S_3 = u\sigma_{13} + v\sigma_{23} + w\sigma_{33} - q_3$$

and

$$\sigma_{ij} = 2\mu\frac{\partial u_i}{\partial x_j} - \frac{2}{3}\mu\frac{\partial u_k}{\partial x_k}\delta_{ij},\ q_i = -k\frac{\partial T}{\partial x_i}$$

In the above equations, p and T are the pressure and temperature, respectively. The working fluid air is considered as thermally perfect gas and the relationship between pressure and temperature is given by the ideal gas law. The dynamic molecular viscosity is obtained using the Sutherland law: $\mu = \mu_0(\frac{T}{T_0})^{3/2}\frac{(T_0+110.4)}{(T+110.4)}$ with $\mu_0 = 1.711\times10^5 \mathrm{kg{\cdot}m^{-1}{\cdot}s^{-1}}$ and $T_0 = 273.15\mathrm{K}$. Flux terms in the other two directions, i.e. G and G_v, H and H_v, are in similar form to F and F_v, and thus are not given for simplicity.

The in-house code OPENCFD-SC is employed to perform the DNS in the present work. This code has been widely applied to a series of studies involving SWTBLIs in a compression ramp [12], hypersonic boundary layer transition over a blunt cone [13]. The inviscid terms are solved using a bandwidth-optimized fourth-order weighted essentially non-oscillatory (WENO) scheme [14] with the Steger-Warming vector flux splitting method. By employing a limiter technique based on the total variation, the numerical dissipation is greatly reduced so that turbulence in smooth regions can be accurately captured. An eighth-order central difference scheme is used to calculate the viscous flux terms. The time integration is performed using the third-order Runge-Kutta method. More details about the numerical method can be found in [12–14].

2.2. Simulation setup

The inflow parameters are similar to those used in the DNS by Priebe et al. [10]. The Mach number and the static temperature of the free-stream flow are $M_\infty = 2.9$ and $T_\infty = 181$ K, respectively. The Reynolds number based on the momentum thickness of the boundary layer is $Re_\theta = 2300$. As shown in Fig. 1, the computational domain is partitioned into two zones. A zero pressure gradient flat-plate boundary layer extends from $x = -365$ mm to $x = 0$ mm, followed by an expansion corner ranging from $x = 0$ mm to $x = 100$ mm. The flow direction is from the left to the

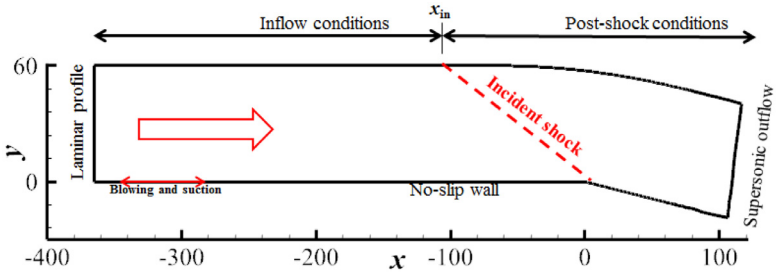

Fig. 1. Schematic of the computational domain and boundary conditions.

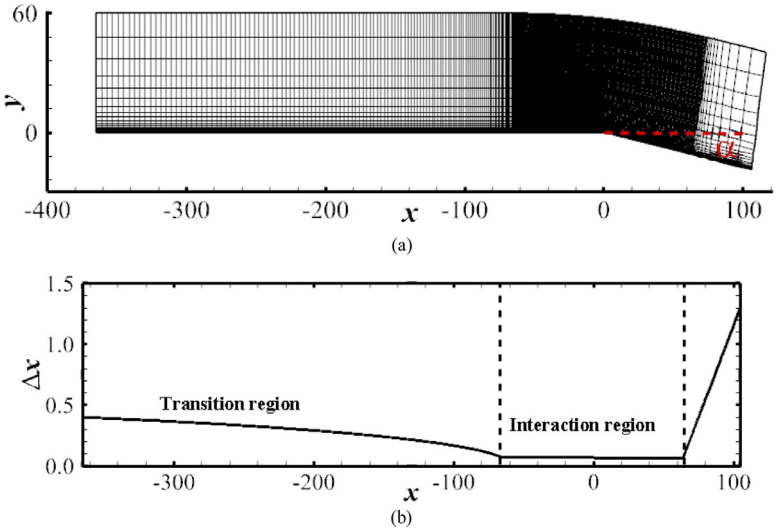

Fig. 2. Sketch of (a) computation grid and (b) streamwise grid spacing. The grid points are plotted at an interval of every ten points in both streamwise and wall-normal directions.

right in this figure. The streamwise length L_x and the wall-normal length L_y are about 460 mm and 60 mm, respectively. The width in the spanwise direction is L_z = 14 mm.

The boundary conditions are imposed as follows. At the domain inlet, a steady laminar profile is imposed, which is obtained from an additional laminar simulation with similar inflow conditions. To obtain a supersonic turbulent boundary layer upstream of the expansion corner, the laminar-transition-turbulent method is used to trigger the laminar flow. A region of blowing and suction is added on the wall, extending from x = -335 mm to x = -315 mm. The wall-normal velocity disturbance is defined as $V_{bs} = AU_\infty f(x)g(z)h(t)$, where A=0.2 is the disturbance amplitude and U_∞ is the free-stream velocity. For more details about the disturbance parameters, readers can refer to the direct numerical simulation of a spatially evolving supersonic turbulent boundary layer by Pirozzoli *et al.* [15]. The incident shock wave is generated by applying the inviscid Rankine-Hugoniot jump conditions on the upper boundary, without considering the effects of geometries and shock generators. The incident location on the upper boundary is set at x_{in} = -104 mm. In the current simulation, the flow deflection angle Φ through the shock is about 12^0. Based on the inflow conditions, the extrapolated point of the incident shock is at x = 0 mm, which is just at the onset of the expansion corner. In addition, the no-slip and isothermal boundary conditions with a wall temperature T_w = 307K are used for the wall. To avoid the reflection of disturbance waves, a non-reflecting boundary condition [16] with the sponge layer [15] is applied at the domain outlet. In the spanwise direction, a periodic boundary condition is applied.

The computation grid employed in the simulation is shown in Fig. 2(a). Compared with the coarse grid spacing in the transition region upstream, grids in the interaction region are significantly refined and distributed with equal spacing in the streamwise direction, as shown in Fig. 2(b). A sponge region with gradually coarsened grid is placed at x > 35 mm to eliminate disturbance reflection from the outlet. The grids are clustered in the near wall region and equally distributed in the spanwise direction. A total of four DNS cases with the same domain size and grid resolution are performed for this study, listed in Table 1. IN-0 is the baseline case, corresponding to the interactions between an incident shock wave and a flat-plate turbulent boundary layer, and it is compared with previous experimental data and DNS results for validation. The other three cases, i.e. IN-2, IN-5 and IN-10, are SWTBLIs near an expansion corner with fixed impingement location for three different expansion angles, i.e. $\alpha = 2^0$, 5^0 and 10^0, respectively. Table 2 lists the parameters of a fully developed supersonic turbulent boundary layer at the reference location ($x = -60$ mm). Unless otherwise stated, variables δ, $\delta^*$and θ in this paper denote the nominal thickness, displacement thickness and momentum thickness at the reference location, respectively. The present incoming turbulent boundary layer is close to the one studied by Priebe et al. [10], except for a slightly higher skin-friction coefficient in the present study.

Based on wall units at x = -60 mm, the streamwise and spanwise grid spacing in the interaction region are $\Delta x^+ = 5.2$ and $\Delta z^+ = 7.5$, respectively. In the wall-normal direction, the grid spacing just above the wall is $\Delta y_w^+ = 0.7$ and about 50 nodes are distributed inside the turbulent boundary layer. It is noticed that this grid resolution is comparable to that used by Priebe et al. [10]. To assess the spanwise domain size, Fig. 3 shows two-point autocorrelations of velocity fluctuations as a function of the spanwise

Table 1
Parameters for the DNS cases studied.

Case	M_∞	Φ (deg)	α (deg)	$(L_x \times L_y \times L_z)/\delta$	$N_x \times N_y \times N_z$	$\Delta x^+ \times \Delta y_w^+ \times \Delta z^+$
IN-0	2.9	12.0	0.0	71.54 × 9.23 × 2.15	3200 × 200 × 140	5.2 × 0.7 × 7.5
IN-2	2.9	12.0	2.0	71.54 × 9.23 × 2.15	3200 × 200 × 140	5.2 × 0.7 × 7.5
IN-5	2.9	12.0	5.0	71.54 × 9.23 × 2.15	3200 × 200 × 140	5.2 × 0.7 × 7.5
IN-10	2.9	12.0	10.0	71.54 × 9.23 × 2.15	3200 × 200 × 140	5.2 × 0.7 × 7.5

Table 2
Parameters for the supersonic turbulent boundary layer at the reference location.

Case	M_∞	$T_\infty(k)$	δ (mm)	δ^* (mm)	θ (mm)	C_f
x = −60 mm	2.9	108	6.5	2.06	0.41	0.00246
Priebe et al. [10]	2.9	107	6.4	1.80	0.38	0.00217
Bookey et al.[11]	2.9	108	6.7	2.36	0.43	0.00225

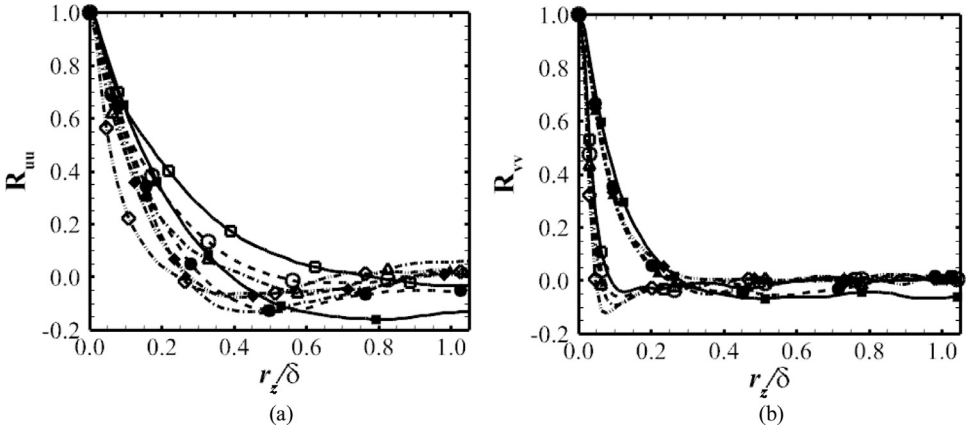

Fig. 3. Two-point autocorrelation of velocity fluctuations as a function of spanwise space at $x = 17$ mm: (a) streamwise velocity; (b) wall-normal velocity. Open symbols: $y/\delta = 0.03$; solid symbols: $y/\delta = 0.6$. Squares: IN-0; circles: IN-2; deltas: IN-5; diamonds: IN-10.

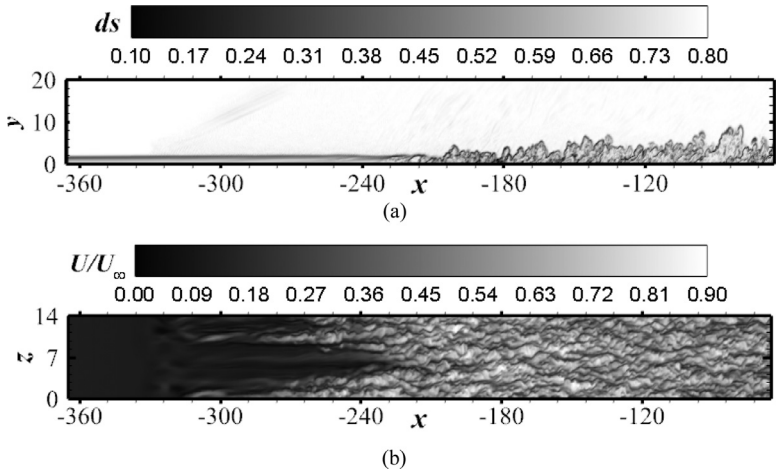

Fig. 4. Instantaneous flow fields in the transition region: (a) density gradient in the x-y plane; (b) streamwise velocity in the x-z plane at $y^+ = 10$.

distance in the interaction region. It is clear that all correlations decrease rapidly towards zero within half the domain width, indicating that the domain width is large enough for the present study.

2.3. Incoming supersonic turbulent boundary layer

Fig. 4 shows the instantaneous fields of the density gradient and the streamwise velocity in the transition region. The density gradient (ds) is defined as $ds = 0.8e^{-10(|\nabla\rho|-|\nabla\rho|_{min})/(|\nabla\rho|_{max}-|\nabla\rho|_{min})}$, similar to Wu & Martin [17]. At $x > -150$ mm, irregular turbulent bulges are clearly visible and the flow fields are characterized by typical elongated streaky structures, indicating that the flow is approaching a fully developed turbulent state.

To further check the incoming turbulent boundary layer, first- and second-order turbulence statistics at the reference location ($x = -60$ mm) are shown in Fig. 5. The van Direst-transformed mean velocity profile in inner scaling is shown in Fig. 5(a), and DNS data by Priebe et al. [10] are also included for comparison. Clearly, the agreement is satisfactory that a linear law is attained for $y^+ < 7$ and the region for $40 < y^+ < 100$ is characterized by a logarithmic scaling. Fig. 5(b) shows the root mean square (RMS) of wall density scaled velocity fluctuations. According to Morkovin's hypothesis, the present compressible DNS results show

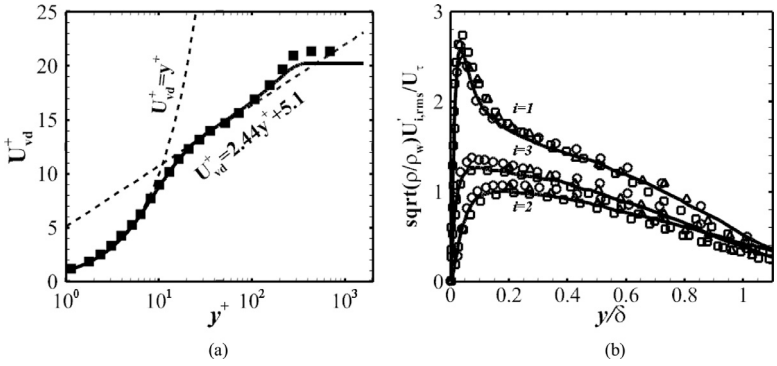

Fig. 5. Statistics of incoming supersonic turbulent boundary layer at $x = -60$ mm: (a) mean velocity profile in inner scaling; (b) RMS of velocity fluctuations in outer scaling. Black solid lines: present data; solid diamonds: Priebe et al. [10]; open squares: Wu & Moin [18]; open deltas: Erm & Joubert [19]; open circles: Pirozzoli & Bernardini [20]. $i = 1, 2, 3$ correspond to streamwise, wall-normal and spanwise components, respectively.

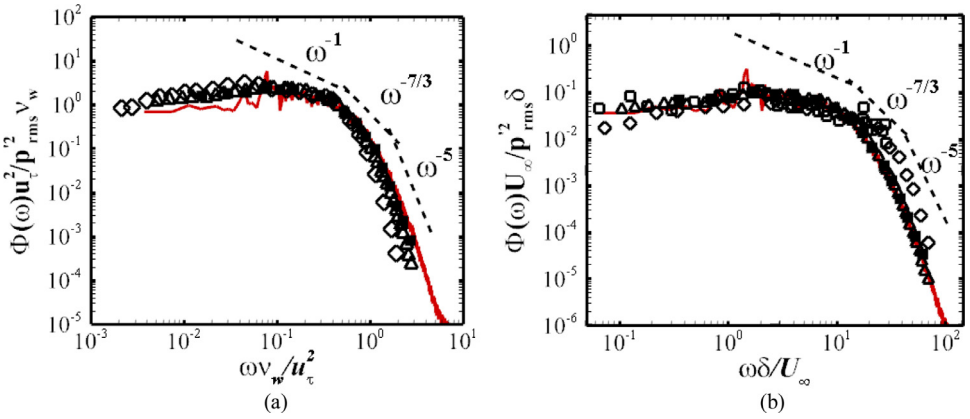

Fig. 6. Wall pressure frequency spectrum in (a) inner and (b) outer scaling at $x = -60$ mm. Red solid lines: present data; open deltas: Duan et al. [21]; solid squares: Bernardini et al. [22]; open squares: Beresh et al. [23]; open diamonds: Farabee & Casrella [24]. (For interpretation of the references to color in this figure legend, the reader is referred to the web version of this article.)

good agreement with previous experimental and numerical data of turbulent boundary layers [18–20]. In addition, Fig. 6 shows the wall pressure frequency spectrum with respect to the inner and outer scaling. For a better comparison, the experimental data of Farabee & Casarell [24] and Beresh et al. [23] and the compressible DNS data of Duan et al. [21] and Bernardini et al. [22] are also plotted together. A remarkable agreement is observed. Consistent with the analysis of Bull [25], the spectrum is reasonably close to ω^{-5} in the high frequency range, associated with the sublayer dominance. Further, in the middle frequency range, the ω^{-1} and $\omega^{-7/3}$ dependence of the pressure spectrum is observed, relating to pressure-inducing eddies in the logarithmic and overlap regions, respectively. The above analysis confirms that a fully developed supersonic turbulent boundary layer has already achieved at the reference location.

3. Flow structures and length scales

3.1. Instantaneous and mean flow fields

Fig. 7 shows instantaneous fields of the density gradient in the x-y plane at $z = 7$ mm (middle plane in the spanwise direction), where the sonic line and iso-line ($u = 0$) are also included for better comparison. Consistent with numerical findings by Priebe et al. [10] for the interactions between a fully developed supersonic turbulent boundary layer and an incident shock, the complex shock system contains an incident shock, a reflected shock, as well as a series of compression waves in the downstream region. It is seen that the strength of compression waves is dramatically reduced, due to the favorable pressure gradient induced by the expansion corner. The flow field also highlights a significant reduction of the separation bubble's size, such that the reflected shock moves closer to the expansion corner, indicating a decrease of the interaction length as the expansion effect get stronger. A more complete quantitative analysis about this will be discussed later. In addition, we can observe that the sonic line moves closer to the wall with the increasing expansion angle, especially for IN-10, suggesting that the inner region of the turbulent boundary layer on the expansion corner is mainly featured by supersonic flows.

The expansion effect on coherent vortex structures in the interaction region is visualized in terms of iso-surfaces of the Q criterion [26]. The coherent vortex structures for IN-0 and IN-10 are shown in Fig. 8(a) and (b), respectively. Here, the iso-surfaces are shown with $Q/Q_{max} = 0.01$ and colored by the wall-normal distance y_n. In the undisturbed boundary layer, numerous streamwise elongated hairpin-like vortices are clearly seen in the outer layer, while the near-wall region is characterized by small-scale vortices closely resembling those in previous DNS studies of compressible turbulent boundary layers [27]. It is noticed that coherent vortex structures are remarkably strengthened after passing through the separation shock for both cases, especially in the separated shear layer above the separation bubble, as also observed in the compression ramp interaction studied by Wu & Martin [17]. However, utterly different response of vortex structures in the reattachment region can be clearly observed. Vortex structures for IN-10 are significantly weakened and dominated by large-scale vortices much closer to the wall. With increasing angle of the expansion corner, the bubble size induced by the shock interaction

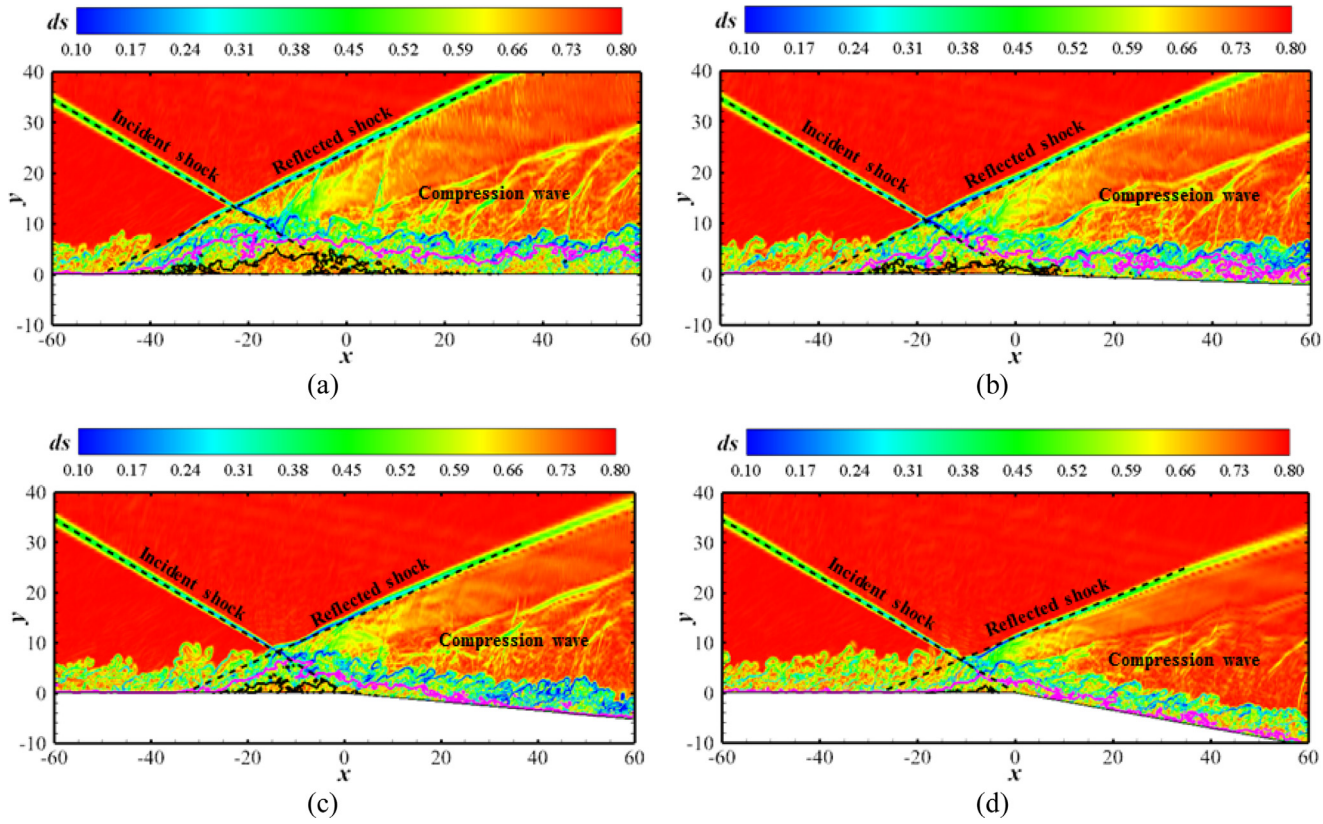

Fig. 7. Instantaneous density gradient fields in the x-y plane at $z = 7$ mm for: (a) IN-0; (b) IN-2; (c) IN-5; (d) IN-10. Black and pink lines correspond to the iso-line ($u = 0$) and sonic line, respectively. (For interpretation of the references to color in this figure legend, the reader is referred to the web version of this article.)

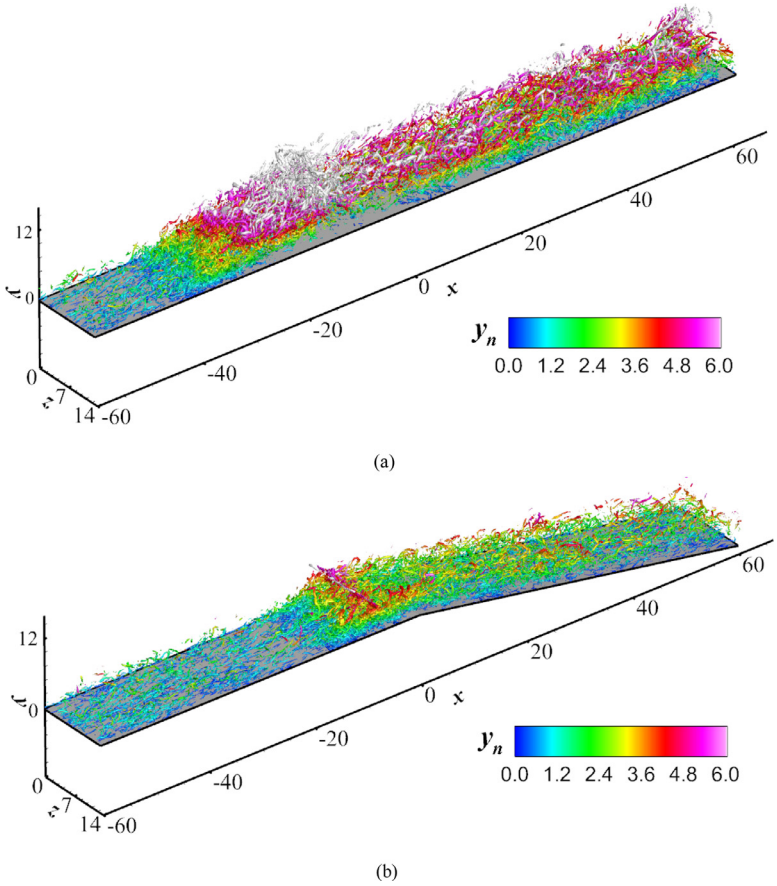

Fig. 8. Iso-surface of the Q criterion ($Q/Q_{max} = 0.01$) in the interaction regions, colored with the wall-normal distance y_n for: (a) IN-0; (b) IN-10.

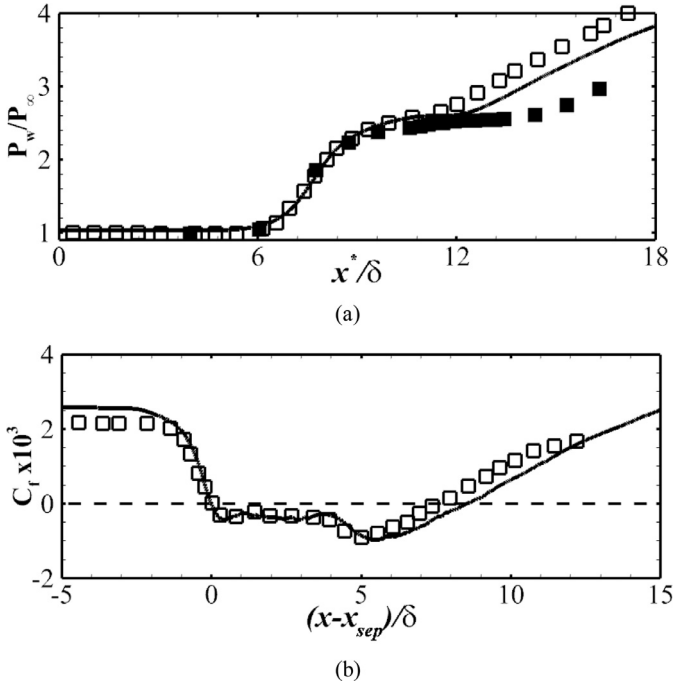

Fig. 9. Distributions of (a) wall pressure and (b) skin-friction coefficient for IN-0. Black solid lines: present data; open circles: DNS data of Priebe et al. [10]; black solid squares: experimental data of Bookey et al. [11].

reduces dramatically and the associated shear layer is also strongly weakened (see Fig. 7). There is a rapid quenching of small-scale vortices in the near-wall region around the expansion corner, which is in excellent agreement with the experimental findings of the structural response to convex curvature in a hypersonic turbulent boundary layer [28].

The distributions of the mean wall pressure and the skin-friction coefficient for IN-0 are compared with the DNS data of Priebe et al. [10] and experimental measurements of Bookey et al. [11], in Fig. 9. Without specification, the mean statistics are obtained by time and spanwise average. Note that the experimental data are extracted along the interaction center within the largest separation bubble, but the exact reference location is unknown. Therefore, similar to Priebe et al. [10], the streamwise coordinate x^*, as shown in Fig. 9(a), is shifted to match the initial pressure rise in the experiment. In Fig. 9(b), the skin-friction profiles obtained by DNS are shifted to the separation point and normalized by the boundary layer thickness. A satisfactory agreement between the numerical and experimental results appears in the region $x^*/\delta < 12$, where the initial pressure rises. Some noticeable discrepancies appear in the second pressure rise and the separation length L_{sep}. Here, the separation length is defined as $L_{sep} = x_{sep}$-x_{ret}, with x_{sep} and x_{ret} being the separation and reattachment points, where the mean skin-friction is zero. Based on the skin-friction profiles in Fig. 9(b), the present separation length is $L_{sep}\approx 8.3\delta$, slightly larger than $L_{sep}\approx 7.6\delta$ in Priebe's DNS data. Due to different turbulence generation methods, global properties of the incoming turbulent boundary layer in the present studies (see Table 2), cannot be exactly the same as those of Priebe et al. [10]. This results in a thinner velocity profile at the reference location, which might be responsible for the discrepancy in the obtained separation region length. In the meantime, we notice that both values from numerical simulations are much smaller than the experimental measurement by Bookey et al. [11], i.e. $L_{sep}\approx 10.5\delta$. The main reason for this discrepancy is likely due to the spanwise periodic boundary conditions used in simulations, where the wind-tunnel side-wall and spanwise length of the shock generator can have serious effects on the experimental data.

Fig. 10(a) exhibits the influence of the expansion corner on the distribution of the mean wall pressure. Clearly, the expansion corner shifts the initial pressure rise downstream, while the streamwise pressure gradient remains almost unchanged. This suggests that although the location of the separated shock is significantly changed due to the expansion, the effect on the shock strength is negligible. Moreover, in the reattachment region, the expansion corner produces a rapid decrease of wall pressure, attaining a minimum value of 2.6 at $x = 60$ mm for IN-10 (60% of the value for IN-0). The skin-friction coefficient distributions for all four cases are compared in Fig. 10(b). With increased expansion effect, an overall rise of the skin-friction occurs at the expansion corner. The separation points move downstream, while the reattachment points exhibit an opposite trend. For all three cases with the expansion corner, flow separations are found in the mean flow. As shown in Fig. 11, the separation length (L_{sep}) significantly decreases as the expansion angle is increased, i.e. from $L_{sep}\approx 8.3\delta$ for IN-0 to $L_{sep}\approx 2.2\delta$ for IN-10. Apparently, the separation point is more responsible for the separation length reduction than the reattachment point. Another interesting feature is the existence of double minima on the skin-friction curves inside the separation bubble. Moreover, the first minima is shifted downstream, consistent with the downstream movement of the initial pressure rise as shown in Fig. 10(a). As the expansion angle increases, the magnitude of the second minima dramatically decreases, while its location is almost unchanged. It is likely that

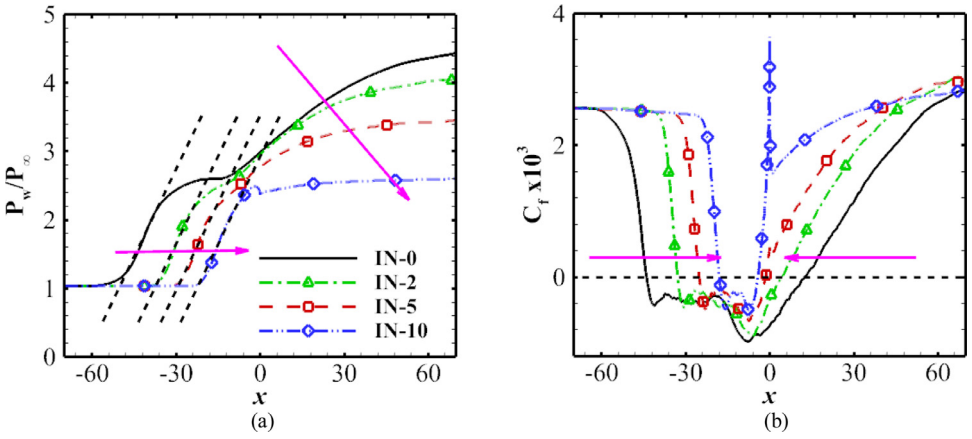

Fig. 10. Expansion effect on the distribution of (a) mean wall pressure and (b) mean skin-friction cofficient.

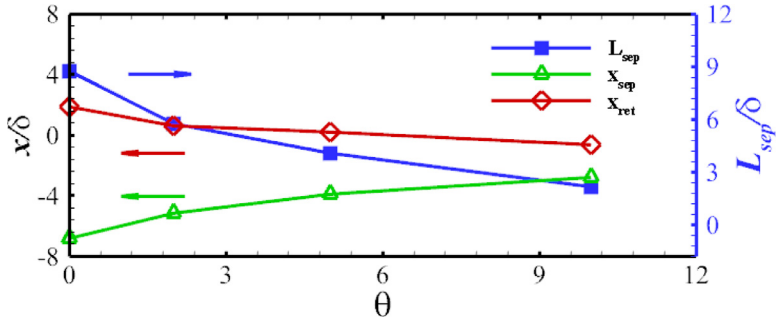

Fig. 11. Distribution of separation length as a function of expansion angle. Open green deltas: separation point; open red diamonds: reattachment point; solid blue squares: mean separation length. (For interpretation of the references to color in this figure legend, the reader is referred to the web version of this article.)

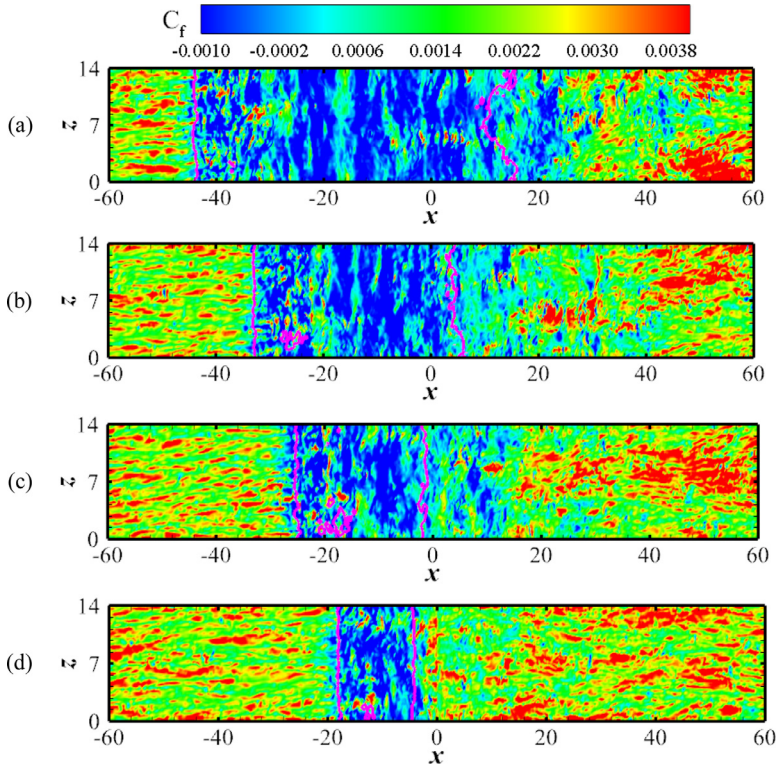

Fig. 12. Contours of instantaneous skin-friction coefficient distribution: (a) IN-0; (b) IN-2; (c) IN-5; (d) IN-10. Pink lines denote the iso-lines of time-averaged $C_f = 0$.

the fixed nominal shock-impingement point at $x = 0$ contributes to the insensitivity of the location change of the reattachment point. Overall, the expansion leads to a smaller separation region.

Further insight into the separation region is shown in Fig. 12 for the contours of skin-friction coefficient, as well as time-averaged separation and reattachment lines (defined by $C_f = 0$). Upstream the separation line, structures are characterized by typical streaky patterns, consistent with previous results for the zero-pressure gradient flat-plate. These streaky structures are completely destroyed in the separation region, but reappear in the recovery region downstream the reattachment line. Compared to the case without expansion, it can be seen that a quicker recovery of streaks is present in the case of larger expansion angles. Moreover, negative flow patches frequently appear between the separation and reattachment lines, indicating strong intermittency of the separation bubble. The separation region is quasi-two-dimensional, and the streamwise size varies significantly with the expansion angle. The expansion effect is better revealed in the spanwise distribution of the reattachment line. For IN-0, there is a significant spanwise variation of the reattachment line, while it is shifted upstream and becomes more regularized with the strengthening of the expansion effect. This indicates that the spanwise modulation in the interaction region is largely suppressed in the presence of the expansion corner, as the flow acceleration damps turbulence activities.

To better characterize the response of the flow intermittency to the expansion corner in the separation region, the statistical probabilities for backflow, i.e. negative $\partial u/\partial y_n$, are quantitatively compared in Fig. 13. Simpson [29] firstly proposed such a classification of separated flow: the instantaneous backflow with a probability of 1%, 20% and 50% is termed as incipient detachment (ID), intermittent transitory detachment (ITD) and transitory detachment (TD), respectively. We can see a doubled-humped distribution for the probability profiles, with one peak located just after the separation point and the other one before the reattachment point, in good agreement with the skin-friction distribution in the interaction region shown in Fig. 10(b). These two peaks on each probability profile are both higher than 20% for all four cases, suggesting that the separation is characterized by transitory detachment. It is also instructive to see that the probability variation exhibits a similar trend to that of the skin-friction distribution as the expansion angle is increased, as indicated by pink arrows in Fig. 13. Another important feature present in the recovery region is

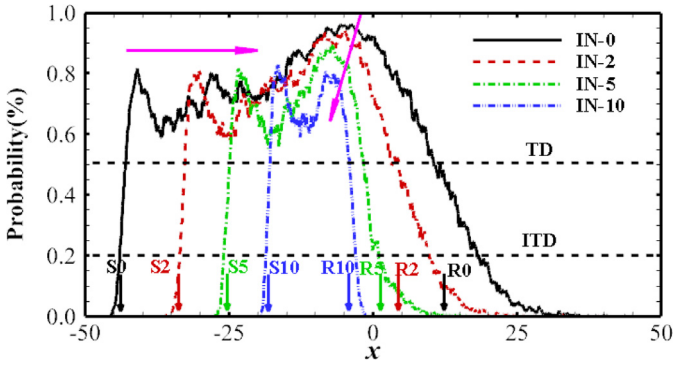

Fig. 13. Statistical probability for reversal flow on the wall (negative $\partial u/\partial y_n$). TD: transitory detachment; ITD: intermittent transitory detachment. Symbols 'S' and 'R' denote the mean separation and reattachment points, respectively. Numbers represent the corresponding expansion angle.

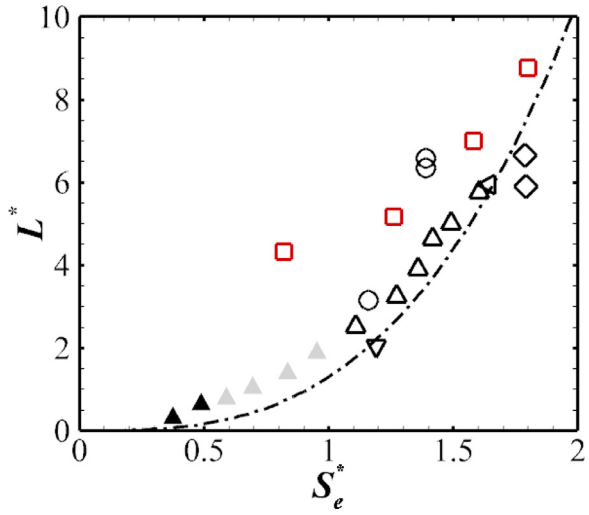

Fig. 14. Distribution of the interaction length L^* as a function of separation criterion $S_e{}^*$. Open red squares: present DNS data; squares: Ringuette et al. [33]; left triangles: Gannapthisubramani et al. [34]; plus: Touber & Sandham [35]; circles: Polivanov et al. [36]; deltas: Laurent [37]. The colors denote the separation state: black, attached; grey, incipient; white, separated. Dash-dotted line denotes the best fit line ($1.3x^3$). (For interpretation of the references to color in this figure legend, the reader is referred to the web version of this article.)

that the transitory detachment is still significant for IN-0 and IN-2, while the intermittent transitory detachment plays the dominant role for IN-5 and IN-10 within a relatively short region.

3.2. Length-scale analysis of the interaction region

To collapse the length scales of interaction regions under different geometries and various flow conditions, Souverein *et al.* [30] firstly proposed a scaling law for the characteristic length of SWTBLIs based on the law of mass conservation. The combined effect of Mach number, Reynolds number and different geometric configurations (incident shock reflection and compression ramp) are all taken into account in a non-dimensional form, which is defined as

$$L^* = \frac{L}{\delta^*}\frac{\sin(\beta)\sin(\phi)}{\sin(\beta-\phi)} = \frac{\dot{m}^*_{out}}{\dot{m}^*_{in}} - 1 \tag{3}$$

where L is the characteristic length of the interaction region defined as the distance between the foot of the reflected shock and the nominal impingement point of the incident shock, β and Φ the shock angle and the flow deflection angle, respectively. Here, the mass-flow deficit $\dot{m}^*$ is defined as $\rho U\delta^*$ with the subscript *out* and *in* for the outflow and inflow conditions, respectively. Souverein et al. [30] suggested that the interaction length was a direct result of the mass-flow deficit ratio between the incoming and outgoing boundary layer. Another important parameter in such a scaling analysis is the separation state criteria

$$S^*_e = \frac{2\bar{k}}{\gamma}\frac{\left(\frac{P_3}{P_1}\right)-1}{M^2_\infty}, \tag{4}$$

where P_3/P_1 denotes the ratio of pressure across the shock system, γ the specific heat ratio. The chosen constant $\bar{k}$ is 3.0 for $Re_\theta \le 1\times10^4$ and 2.5 for $Re_\theta > 1\times10^4$, where $Re_{\theta,}$ is the Reynolds number based on the momentum thickness of the incoming turbulent boundary layer. Subsequently, Jaunet et al. [31] experimentally investigated the wall temperature effect on the length scales of the heated SWTBLIs, thus the heating effects on the skin-friction coefficient are correctly considered to improve the accuracy.

Recently, Quadros and Bernardini [32] found that the above scaling analysis of turbulent interactions is still applicable to transitional interactions. In this section, we validate whether such a scaling analysis can also be applied for the present cases with expansion effect. To do so, we first test the applicability of Eqs. (3) and (4) in the interaction region near an expansion corner, as shown in Fig. 14. For reference purpose, previous numerous experimental and numerical results with a wider range of flow conditions are also plotted together. Moreover, the associated parameters for all four cases are summarized in Table 3 for comparison. According to the classification based on the non-dimensional scaling proposed by Souverein et al. [30], L^* <1 corresponds to interactions with attached flow, L^* >2 separation interactions and 1<L^*<2 incipient separation. As expected, L^* decreases rapidly with increasing the expansion angle. It can be seen from Table 3 that the value of $L^* = 4.32$ for IN-10, about 49% of that for IN-0, confirming that the interaction states of all the four cases in the present study are completely separated. There is an evident deviation in the presence of the expansion corner, indicating that the imposed expansion effect on the interaction length cannot be neglected. For example, a strong deviation of approximately 520% from the best-fit line appears for IN-10, suggesting that Souverein' scaling law is not equally applicable to the interaction near an expansion corner in the present study.

After a careful examination of the mass conservation and a detailed comparison with previous numerical results, we notice that there exists a noticeable difference between the original incident shock reflection and the present interactions near an expansion corner. Following Souverein's mass-flow balance analysis, we assume that the non-dimensional interaction length can also be interpreted in terms of the mass-flow deficit ratio. However, as an expansion corner is present, an additional term $\rho_3U_3\sin\alpha/\rho_1U_1$ in the trigonometrical correction factor is also taken into account to approximate the expansion effect, thus a modified dimensionless form of the interaction length is proposed as below,

$$L^*_m = \frac{L}{\delta^*_0}\left(\frac{\sin\beta\sin\phi}{\sin(\beta-\phi)} - \frac{\rho_3U_3}{\rho_1U_1}\sin\alpha\right) \approx \frac{\dot{m}^*_{out}}{\dot{m}^*_{in}} - 1. \tag{5}$$

Note that mass-flux ratio ρ_3U_3/ρ_1U_1 cannot be determined algebraically, thus it is numerically evaluated from the simulation, as shown in Fig. 15(a). As expected, the profiles exhibit a considerable decrease of mass-flux ratio. Using this newly modified scaling, a satisfactory agreement with the best-fit line is thus achieved in Fig. 15(b). However, more DNS cases are still needed to further validate the applicability of the new scaling.

Table 3
Parameters for the scaling analysis of the interaction length.

Case	α(deg)	Φ(deg)	β(deg)	L/δ^*	L^*	L_m^*	S_e^*	$\rho_3 U_3/\rho_1 U_1$	P_3/P_1
IN-0	0	12	28	24.76	8.77	8.77	1.73	2.27	4.43
IN-2	2	12	28	19.80	7.01	5.50	1.60	2.18	4.15
IN-5	5	12	28	14.61	5.17	2.59	1.24	2.02	3.43
IN-10	10	12	28	12.21	4.32	0.68	0.81	1.72	2.59

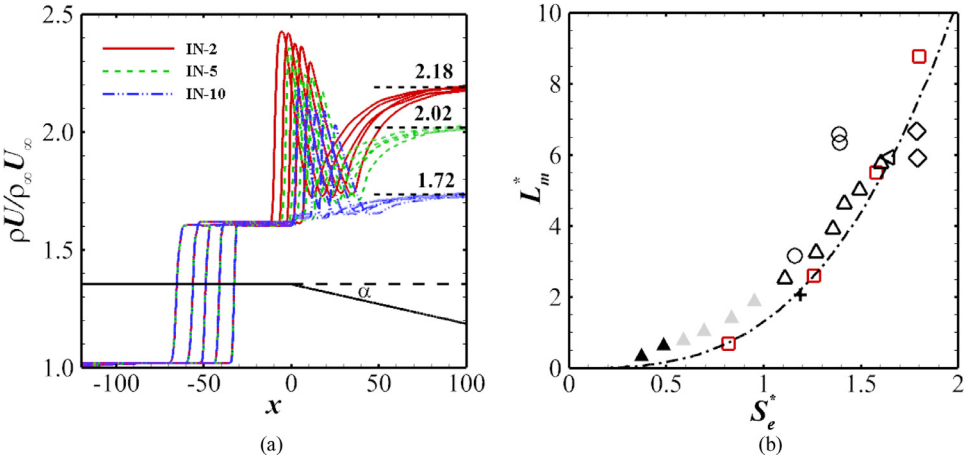

Fig. 15. (a) Distribution of mass-flux ratios ($\rho U/\rho_\infty U_\infty$) across the interaction; (b) modified scaling for the interaction length under expansion. Symbols and line are the same as in Fig. 14.

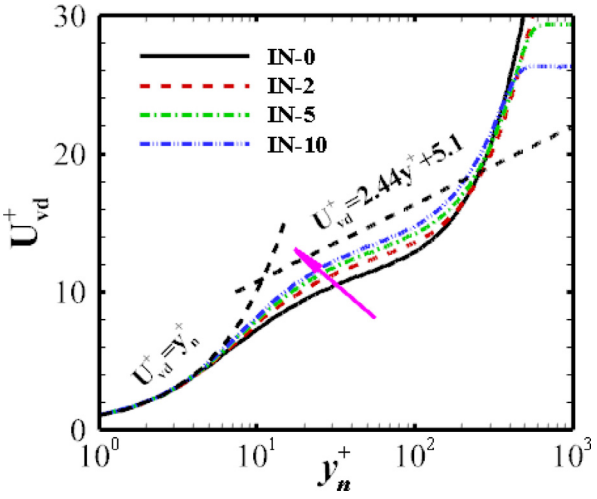

Fig. 16. The van-Driest transformed mean velocity as a function of wall-normal distance normalized by local inner units. The data is taken at x = 30 mm.

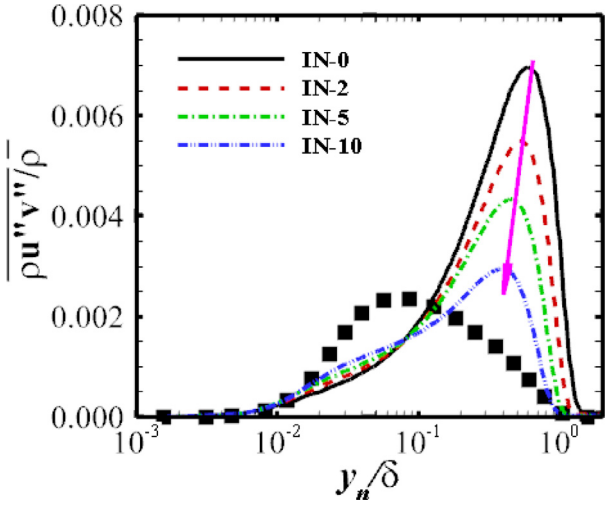

Fig. 17. Reynolds shear stress as a function of wall-normal distance normalized by outer units at x = 30 mm. Black solid squares are data taken at the reference location.

4. Statistics of the post-shock turbulent boundary layer

In this section, effects of the expansion corner and the shock wave interaction on the statistical characteristics of the post-shock turbulent boundary layer are analyzed. For a better comparison, turbulence statistics on the expansion corner are all extracted at x = 30 mm. A total of 400 instantaneous flow fields spanning three flow-through times are used to ensure the statistical convergence.

4.1. Mean velocity and Reynolds shear stress

Fig. 16 plots the van-Driest transformed mean velocity profiles as a function of wall-normal distance in inner scaling. No significant difference is observed in the viscous sub-layer, i.e. $y_n{}^+ < 10$, where a linear scaling is approximately preserved for all cases. However, statistical behaviors in the logarithmic region are dramatically changed by combined effects of the shock wave interaction and the expansion corner. A characteristic dip, closely resembling the finding in cases of reflected shock interactions [10] and compression ramps [17], is evidently highlighted on the expansion corner, suggesting that the disturbed turbulent boundary layer is still out of the equilibrium state. Theexpansion effect on the mean velocity profile is to make it gradually approach the log-law for $10 < y_n{}^+ < 100$.

Reynolds shear stresses on the expansion corner are shown in Fig. 17 as a function of wall-normal distance in outer units. Here, the density-weighted decomposition of the flow quantity f is used, i.e. $f = \tilde{f} + f'' = \overline{\rho f}/\bar{f} + f''$, with overbar indicating average in time and the spanwise direction, and tilde for density-weighted average. The profile at x=-60 mm, corresponding to the incoming

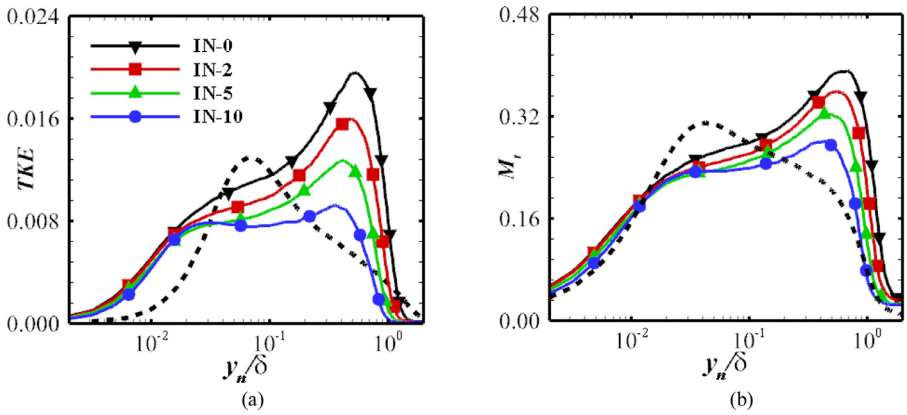

Fig. 18. Profiles of (a) turbulent kinetic energy and (b) turbulent Mach number as a function of wall-normal distance. Dash-line: $x = -60$ mm; Solid lines with symbols: $x = 30$ mm.

fully developed flat-plate turbulent boundary layer, is also included for reference. At a first glance, compared to the incoming boundary layer, the post-shock turbulent boundary layer exhibits a significantly enhanced peak, owing to the shock interactions before the expansion corner. This peak is located in the outer region of the disturbed turbulent boundary layer for all four cases, whereas the incoming boundary layer is apparently dominated by a peak in the near wall region. This might be related to large structures originating from the separated shear layer which present away from the wall. Secondly, as the expansion angle increases, the peak values of the Reynolds shear stress reveal a remarkable decrease. Specifically, the peak value for IN-10 is about 42% of that for IN-0 and just slightly higher than the upstream reference value. From this, we can see that the expansion corner plays an opposite role compared to the shock interaction, especially in the case of large expansion angles, which might mainly relate to the strong favorable pressure gradient imposed by the expansion corner. As a result, the total adverse pressure gradient through the shock wave interaction region is greatly reduced (see Fig. 10a); thus the disturbance energy of the post-shock turbulent boundary layer is much lower and the recovery to the equilibrium state is much faster.

4.2. Turbulent kinetic energy

Fig. 18 shows the turbulent kinetic energy ($TKE, K = 1/2\,\widetilde{u_i''u_j''}$) and turbulent Mach number ($M_t = \sqrt{\overline{u_j'u_j'}}/\bar{c}$) profiles at $x = 30$ mm, respectively. For reference purpose, we also report the incoming boundary layer profiles at $x = -60$ mm. For the zero pressure-gradient boundary layer, it is seen that the peaks of TKE and M_t occur in the near-wall region, at $y_n/\delta \approx 0.07$ and 0.04, respectively. For IN-0, the post-shock boundary layer undergoes a strong amplification due to shock interactions, and those peak values in the downstream region are amplified by a factor of about 1.5 and 1.3 for TKE and M_t, respectively. Clearly, their locations are both moved away from the wall into the outer region of the boundary layer, which might mainly relate to the lift-up of vortex structures, as seen from Fig. 8. In the presence of the expansion corner, both profiles exhibit a similar reduction behavior. Specifically, the TKE and M_t decrease monotonically with increasing the expansion angle, whereas the peak locations are maintained in the outer layer and slightly shifted towards the wall. For IN-10, the peaks are much lower than that of the reference, indicating that the enhancement of turbulence due to shock wave interactions has been completely cancelled out by the downstream expansion effect after the corner. This reduction mechanism might be associated with the significant weakening of large-scale turbulent structures over the expansion corner, as also observed by Sun et al. [38] in supersonic turbulent flow over an expansion corner. Another important mechanism for this phenomenon might be that shedding of vertical structures originating from the weakened shear layer is dramatically attenuated due to the strongly reduced separation bubble size.

To better characterize the expansion effect on the turbulent kinetic energy, various terms in the transport equation of the turbulent kinetic energy, as given by Pirozzoli et al. [20], are systematically analyzed. Fig. 19 shows the budget of the turbulent kinetic energy as a function of wall distance at $x = -60$ mm, compared with the compressible numerical data of Pirozzoli et al. [20] at $Re_\theta = 3530$. All terms in the budget are normalized by the wall quantity $\rho_w u_\tau^4/\nu_w$ and only significant terms in the balance are shown for clarity. The agreement is satisfactory, consistent with typical TKE budget profiles of the flat-plate turbulent boundary layer. In the near-wall region, the production term $P = -\bar{\rho}\widetilde{u_i''u_j''}\partial\tilde{u}_i/\partial x_j$ and the turbulent transport term $T = -\partial[1/2\bar{\rho}\widetilde{u_i''u_i''u_j''} + \overline{p'u_j''}]/\partial x_j$ are relatively small and can be neglected, thus the viscous diffusion $V = \partial(\overline{\sigma_{ij}''u_i''})/\partial x_j$ and the viscous dissipation $\varepsilon = -\overline{\sigma_{ij}''\partial u_i''/\partial x_j}$ dominate the budget. Away from the wall, the budget is characterized by the balance between the turbulent production and viscous dissipation in a large portion of the boundary layer, and the turbulent transport term also becomes insignificant.

Fig. 20(a) shows the wall-normal distribution of the turbulent kinetic energy production on the expansion corner. This figure highlights a typical bimodal structure, whereby the lift-up of vortex structures originating from the separated shear layer causes the first peak in the outer region, while the inner peak is an indicator of flow recovery, as also been observed by Pirozzoli et al. [20] in the case of impinging shock wave/turbulent boundary layer interactions. It is noticed that the production undergoes a different evolution mechanism in the post-shock boundary layer downstream. For IN-0, the turbulent production is mainly attributed to flow structures in the outer part and the maximum value is observed at $y_n/\delta \approx 0.6$, corresponding to the highest turbulent kinetic energy in Fig. 18(a). The second peak with a value of 0.65, about 60% of the maximum production, is attained very close to the wall. Increasing the expansion angle results in a monotonic decay of the turbulent production in the outer region, whereas the production in the inner part exhibits an utter opposite trend. For IN-10, the production profile is characterized by an inner peak and exhibits similarity to the profile at the reference location. The expansion effect on the distribution of the viscous dissipation is shown in Fig. 20(b), and it is mainly reflected in the significant decrease of the leading peak

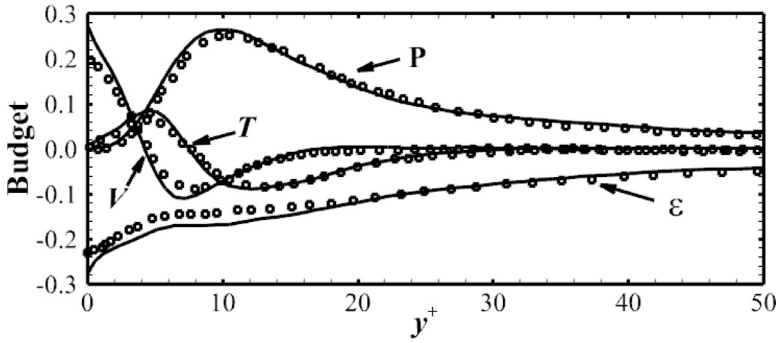

Fig. 19. Budget of turbulent kinetic energy as a function of wall-normal distance at the reference location. Black lines: present DNS data; black circles: DNS data of Pirozzoli & Bernardini [20] at $Re_\theta = 3530$. All terms are normalized by $\rho_w u_\tau^4/\nu_w$.

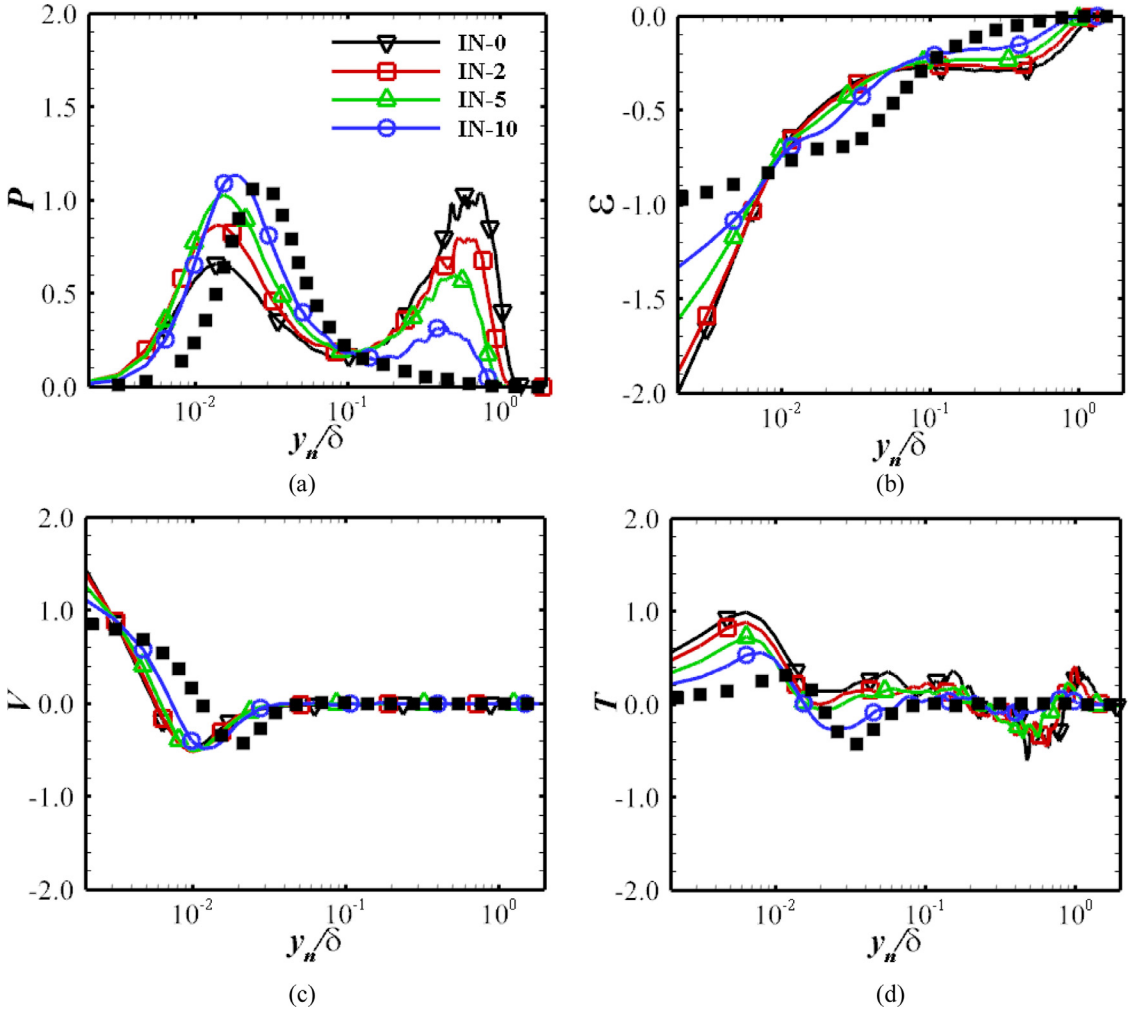

Fig. 20. Turbulent kinetic energy budget terms as a function of wall-normal distance at $x = 30$ mm: (a) turbulent production; (b) viscous dissipation; (c) viscous diffusion; (d) turbulent transport. Black solid squares are data taken at the reference location. All terms are multiplied by 10^3.

in the vicinity of the wall, where strong viscous dissipation is predominant. Overall, the viscous dissipation term is strengthened in the near-wall region and attenuated in the outer region, respectively. As shown in Fig. 20(c), the viscous diffusion plays an important role in the near-wall region, i.e. $y_n/\delta < 0.03$, and the expansion effect on the viscous diffusion is negligible, except a slight decrease in the proximity of the wall. Fig. 20(d) shows the distribution of the turbulent transport in the presence of the expansion corner. It is apparent that the turbulent transport is most significant in the inner region. At larger expansion angle, the flow recovers more quickly to its equilibrium state. Based on the above item-by-term analysis, we can see that the expansion corner has no essential effect on the turbulent kinetic budget of the post-shock turbulent boundary layer, which still remains similar to the incoming turbulent boundary layer, but it plays the role of accelerating the flow, resulting in a much quicker recovery to the equilibrium state.

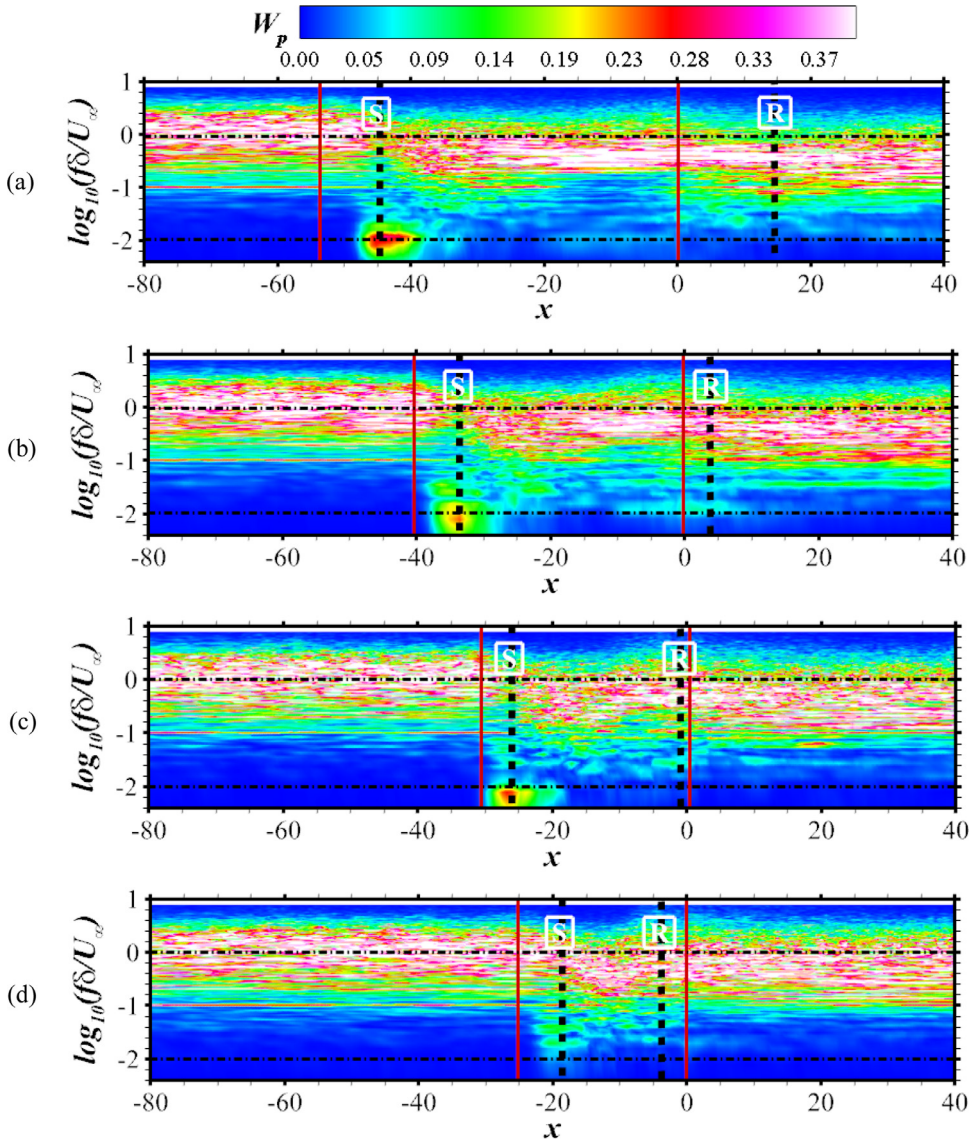

Fig. 21. Weighted PSD of wall pressure fluctuations as a function of streamwise location for: (a) IN-0; (b) IN-2; (c) IN-5; (d) IN-10. The vertical dashed lines denote streamwise locations of the mean separation point ('S') and reattachment point ('R'), respectively. Red boxes indicate regions of interaction. (For interpretation of the references to color in this figure legend, the reader is referred to the web version of this article.)

5. Unsteadiness in the interaction region

In order to quantitatively investigate the influence of the expansion corner and assess possible sources for low frequency shock oscillations, spectral analysis is performed for wall pressure fluctuations. We first study the weighted power spectral density W_p, defined as below,

$$W_p = f * PSD(f) / \int PSD(f)\mathrm{df} \tag{7}$$

here, PSD represents the power spectral density, and is estimated using Welch's method with the Hamming window and 50% overlap. Contour maps of the weighted PSD are shown as a function of streamwise location (x) and frequency ($f\delta/U_\infty$) in Fig. 21. For the four DNS cases considered, wall pressure signals along the spanwise centerline are sampled, where a total of 200 wall probes are evenly distributed along the streamwise direction ranging from $x = -80$ mm to $x = 40$ mm. A constant time interval of about $0.062\delta/U_\infty$ is used for sampling, corresponding to a maximum resolvable frequency of nearly $8.0U_\infty/\delta$. The sampling data is obtained over a time period of about $700\delta/U_\infty$ and divided into 8 segments. The length of each segment is about 4096, leading to a minimum resolvable frequency of about $0.004U_\infty/\delta$.

Fig. 21(a) shows the weighted PSD contour for the case without expansion, and the result is consistent with previous numerical and experimental observations in shock-induced separated flow. Upstream the interaction region, no significant energy is observed at low frequency and the spectra are mainly concentrated around $f\delta/U_\infty$=1.0, corresponding to the most energetic structures in canonical wall-bounded flows. A different behavior appears in the interaction region, especially close to the mean separation point, where high frequency energy levels are dramatically decreased and the spectrum exhibits a dominant peak at a very low frequency of about $f\delta/U_\infty \approx$ 0.007. This is known to be associated with the low frequency oscillation of the separated shock wave [39–42]. According to Eengil & Dolling [43] and Dussauge et al. [44], a dimensionless frequency is defined by $S_L = f_s L_{sep}/U_\infty$, with the frequency of shock motion f_s and the length of the separation bubble L_{sep}. The dimensionless frequency, or Strouhal number, is found to be independent of flow geometry covering a range of Mach number

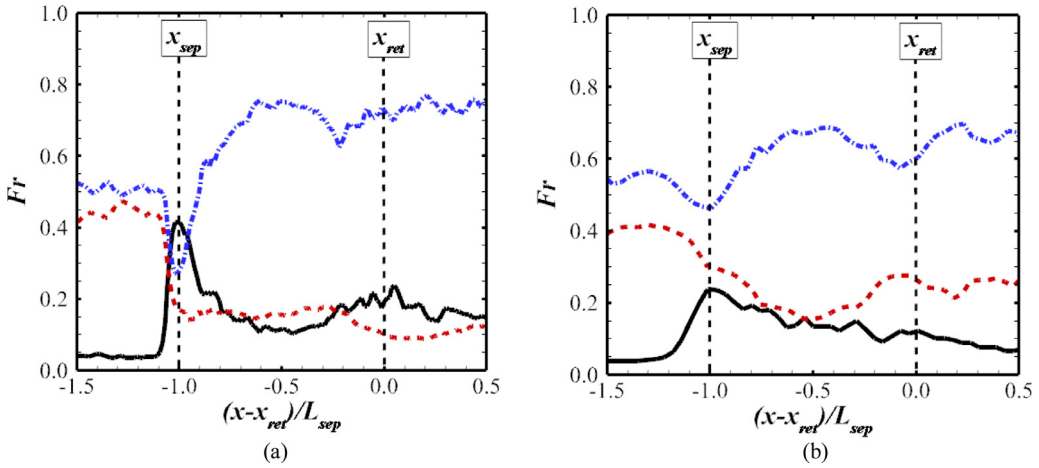

Fig. 22. Band-limited contributions to wall pressure fluctuation as a function of streamwise location: (a) IN-0; (b) IN-10. Black solid lines: $f\delta/U_\infty < 0.1$; blue dash-dot lines: $0.1 < f\delta/U_\infty < 1.0$; red dashed lines: $f\delta/U_\infty > 1.0$. Symbols x_S and x_R denote the mean separation and reattachment points, respectively. (For interpretation of the references to color in this figure legend, the reader is referred to the web version of this article.)

and Reynolds number. Dussauge et al. [44] found that a nearly constant value between 0.02 and 0.05 is obtained for supersonic flow at Mach number larger than 2. Based on the weighted PSD of wall pressure signal at the separation point, the dimensionless frequency in the present study is inferred to a Strouhal number of $S_L = 0.058$. Downstream the interaction region, the spectrum is recovered and characterized by broadband peaks of high frequencies, but slightly lower than that of the incoming flow. Such a behavior is mainly related to the significant strengthening of large-scale vortex structures and the thickening of the boundary layer in the downstream region, which can be seen from Fig. 8(a). As the expansion angle is increased, it is noticed in Fig. 21(b–d) that the low frequency peak at the separation point gradually becomes weak, closely resembling the results by Morgan et al. [45] in the study of shock interactions with a range of shock strengths. As shown in Fig. 21(b and c), the low frequency oscillation of the separated shock wave is still predominant for IN-2 and IN-5. Specifically, the characteristic frequency of shock motion in both cases is approximately estimated to be $0.008U_\infty/\delta$, relatively higher than that of IN-0. Considering the separation length is $L_{\text{sep}} = 5.73\delta$ for IN-2 and $L_{sep} = 3.65\delta$ for IN-5, the corresponding Strouhal number is about 0.046 and 0.03, respectively, showing an obvious decrease of S_L as the expansion angle is increased. In addition, the spectrum shown in Fig. 21(d) illustrates a significant reduction of low-frequency energy and a remarkable amplification at medium frequencies near the mean separation point, implying that there exists essential energy transfer across scales. This also suggests that the unsteadiness in IN-10 is characterized by medium frequencies, as the low frequency unsteady oscillation of the separated shock wave has been completely suppressed. Recalling that all four DNS cases are performed under the same conditions except different angles of the expansion corner, the observed spectra behavior is likely linked with the separation bubble downstream, where the mean flow is moderately separated for IN-10 but strongly separated for IN-2 and IN-5 (Fig. 11). This is similar to the dominant role played by separation bubble pulsations as proposed by Priebe and Martin [40].

The contribution to PSD from different frequency ranges is defined to further quantify the expansion effect, such that

$$Fr = \int_{f_1}^{f_2} PSD(f)\mathrm{d}f/\sigma_{pw}^2, \tag{8}$$

where f_1 and f_2 denote the lower and upper limits of the selected frequency range respectively, and σ_{pw} is the standard deviation of the wall pressure fluctuations, representing the total energy. Here, the resolvable frequency band is divided into three frequency bins, corresponding to low frequencies $0.004 < f\delta/U_\infty < 0.1$, medium frequencies $0.1 < f\delta/U_\infty < 1.0$ and high frequencies $f\delta/U_\infty > 1.0$, respectively. The band-limited contribution as a function of the normalized streamwise coordinate $x^*=(x\text{-}x_{\text{r}})/L_{\text{sep}}$ for IN-0 is plotted in Fig. 22(a). In this coordinate, $x^* = -1$ and 0 refer to the mean separation and reattachment points, respectively. Note that the contribution from the low frequency range is consistent with the observations in Pasquariello's large eddy simulation of impinging shock interactions [46]. Given the lower Reynolds number and weaker shock strengths in the present study, it is not surprising that the maximum faction at $x^* = -1$ is just about 40%, significantly lower than the ratio of 95% in Pasquariello's simulations. However, compared to the contributions from medium and high frequency ranges, it is noticed that the low frequency contribution is still more prominent and plays the leading role. Fig. 22(b) shows the three band-limited contributions for IN-10 in the same manner. Clearly, at the separation point, the contribution from low frequency range significantly decreases and the other two contributions exhibit an opposite behavior. For example, the low frequency contribution attains to a value of approximate 25%, whereas the medium frequency contribution increases to nearly 50% and becomes the driving factor. At $x^* = 0$, it is noticed that the expansion corner has no essential influence on the energy levels and the medium frequency range contributes to most of the energy. Additionally, the contribution from the high frequency range is slightly increased and overtakes the low frequency contribution all the way.

To further assess possible influence of the expansion corner on the unsteadiness in the interaction region, flow fields are quantitatively analyzed using the dynamic mode decomposition (DMD). A brief overview of DMD algorithm is given first. For a given sequence of instantaneous flow fields $\{\psi_0, \psi_1, \cdots \psi_N\}$, , the DMD analysis extracts the dynamically relevant modes Φ_i of a single frequency in a r-dimensional subspace as follow [47]

$$\underbrace{[\psi_0\ \psi_1 \cdots \psi_{N-1}]}_{\Psi} \approx \underbrace{[\phi_1\ \phi_2 \cdots\ \phi_r\ ]}_{\Phi}$$
$$\underbrace{\begin{bmatrix}\alpha_1 & & & \\ & \alpha_2 & & \\ & & \ddots & \\ & & & \alpha_r\end{bmatrix}}_{D_\alpha} \underbrace{\begin{bmatrix}1 & \mu_1 & \cdots & \mu_1^{N-1} \\ 1 & \mu_2 & \cdots & \mu_2^{N-1} \\ \vdots & \vdots & \ddots & \vdots \\ 1 & \mu_r & \cdots & \mu_r^{N-1}\end{bmatrix}}_{V_{and}}, \tag{11}$$

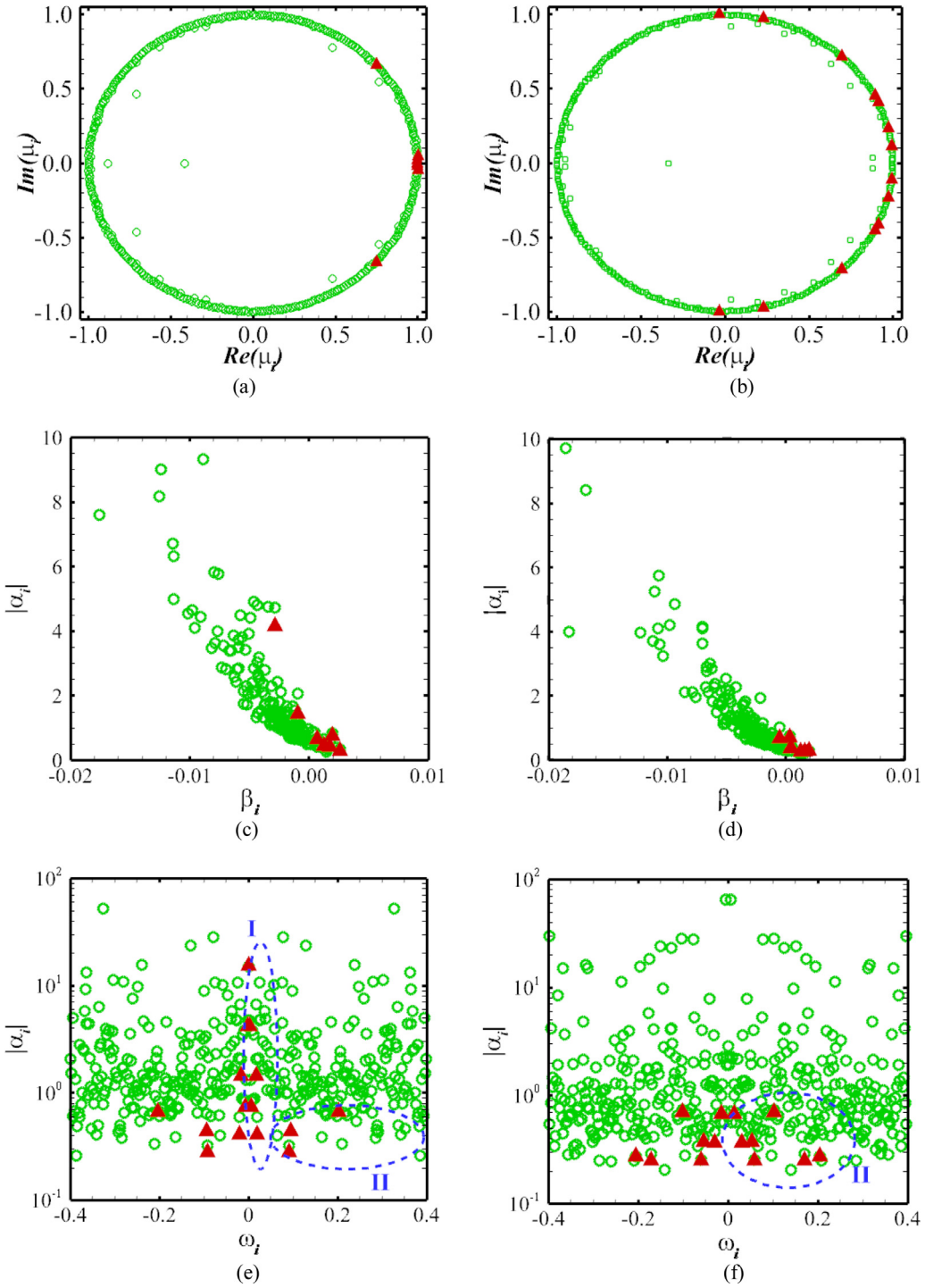

Fig. 23. Standard DMD and DMDSP of streamwise velocity fluctuations for (a, c, e) IN-0 and (b, d, f) IN-10: (a, b) eigenvalues; (c, d) mode amplitude as a function of temporal grow rate; (e, f) mode amplitude as a function of frequency. Greed circles: standard DMD; solid red deltas: DMDSP ($N_{\text{sub}} = 14$). (For interpretation of the references to color in this figure legend, the reader is referred to the web version of this article.)

where α_i and μ_i represent the amplitude and eigenvalue of the DMD mode Φ_{i}, respectively. Using the logarithmic mapping, the temporal growth rate β_{i} and frequency ω_i of Φ_{i} are defined as $\beta_i = \text{Re}(\log \mu_i/\Delta t_s)$ and $\omega_i = \text{Im}(\log \mu_i/(2\pi\,\Delta t_s)$, where Δt_s is the time interval between two adjacent flow fields. In the the present study, a sparsity-promoting DMD method (DMDSP) proposed by Jovanovic et al. [48] is used to identify the most important dynamic modes in the underlying DNS data. According to Jovanovic's algorithm, the automated selection is performed through solving a convex optimization problem written as

$$\underset{\alpha}{minimize}\ ||\sum V^* - YD_\alpha V_{and}||_F^2 + \gamma \sum_{i=1}^{r} |\alpha_i|. \tag{12}$$

Here, the singular value decomposition (SVD) of the snapshot matrix ψ is performed to obtained matrices Σ and V, where $\|\cdot\|_F^2$ and asterisk * denote the Frobenius norm and the complex-conjugate transpose of a matrix, respectively. Note that the

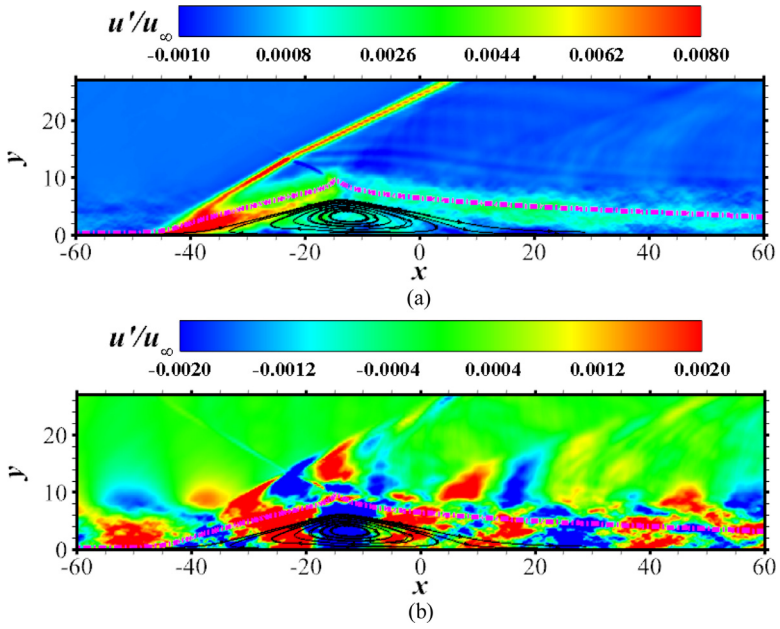

Fig. 24. Real part of the DMDSP modes for IN-0: (a) $f_{\mathrm{I}} = 0.002U_\infty/\delta$; (b) $f_{\mathrm{II}} = 0.2U_\infty/\delta$. Pink dash-dot lines indicate the mean sonic line. The mean separation bubble is shown by the solid black lines.

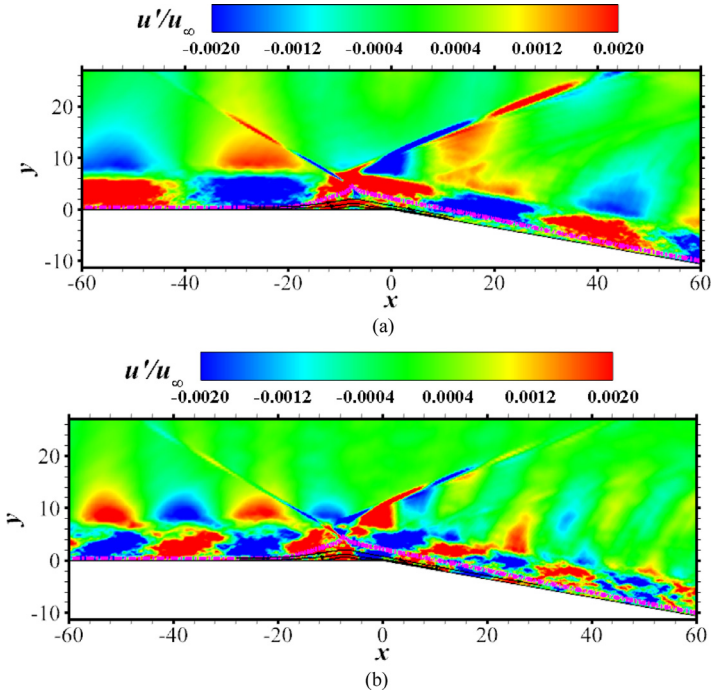

Fig. 25. Same as Fig. 24, but for IN-10: (a) $f_{\mathrm{II}} = 0.1U_\infty/\delta$; (b) $f_{\mathrm{II}} = 0.2U_\infty/\delta$.

user-defined positive value γ is case dependent and reflects the sparsity of the amplitude vector. When $\gamma = 0$, the DMDSP method is identical to the standard DMD method. More detailed description of the DMD and DMDSP analysis can be found in Schmid [47] and Jovanovic et al. [48].

The modal analysis is applied to instantaneous flow fields of spanwise-averaged streamwise velocity fluctuations, as in the studies of Pasquariello et al. [46] and Priebe et al. [49]. To clearly present the expansion effect on the interaction region, a subdomain covering -60 mm $< x <$ 60 mm and $0 < y <$ 27 mm has been stored at a constant time step $\Delta t_{\mathrm{s}} = 1.33\delta/\boldsymbol{U}_\infty$ with 400 snapshots in total. This gives a resolvable frequency bin of $0.002 < f\delta/U_\infty < 0.4$. Compared to the above spectral analysis of the wall pressure, a much lower sampling frequency is chosen here, as the focus is on the low frequency motions.

The expansion effect can be clearly identified by the DMD and DMDSP spectra, displayed in Fig. 23 for IN-0 and IN-10. Based on the sparsity-promoting framework, a subset of $N_{\mathrm{sub}} = 14$ modes, which has strongest influence on the entire evolution process, is extracted by the DMDSP algorithm for both cases. As shown in Fig. 23(a) and (b), most of the DMD modes are distributed along the unit circle for both cases, except that those strongly damped modes appear inside the circle, suggesting that the interaction region is statistically stationary. It is clear that all the selected

dynamically relevant modes only reside on the unit circle. However, the retained modes for IN-0 are apparently concentrated around the point (1, 0), while the distribution for IN-10 has a broadband character. The dependence of the modal amplitude $|\alpha_i|$ on the temporal grow rate β_i is reported in Fig. 23(c) and (d) for IN-0 and IN-10, respectively. As expected, these modes with highest amplitudes are not selected by the DMDSP method due to their strong temporal decay rates and only contributing mostly in the early stage of the entire process. On the contrary, the decay rates of those selected dynamically important modes are nearly zero, responsible for a statistically stationary dynamical system. The dependence of the modal amplitude $|\alpha_i|$ on the frequency ω_i is shown in Fig. 23(e) and (f) for IN-0 and IN-10, respectively. As expected, both DMD and DMDSP modes are symmetrically distributed. Moreover, it can be seen from Fig. 23(e) that the DMDSP modes for IN-0 can be classified into two different types, i.e. type I: a narrow low frequency bin, and type II: a broadband medium frequency bin, indicating a multiple-frequency behavior related to the unsteadiness in the interaction region. This behavior has also been found by Pasquariello et al. [46] for strong shock/turbulent boundary layer interaction at high Reynolds numbers. However, for IN-10 shown in Fig. 23(f), only type II modes are identified and no evidence of dynamically important low frequency modes (type I) can be observed, consistent with the above spectral analysis of wall pressure fluctuations. This confirms that the expansion effect has significant influence on the low frequency unsteady motion in the interaction region.

To deeply investigate the relationship between flow structures and the characteristic frequencies, those dynamical relevant DMDSP modes are examined. Two modes for IN-0 are shown in Fig. 24, i.e. $f_{\mathrm{I}} = 0.002U_\infty/\delta$ for type I modes and $f_{\mathrm{II}} = 0.2U_\infty/\delta$ for type II modes. As a reference, the mean streamlines and the mean sonic line are drawn in the plot to roughly indicate the separation region and the shear layer, respectively. Firstly, there are no significant fluctuations observed in the incoming turbulent boundary, supporting previous downstream mechanism account for the low frequency oscillation. Similar to the observations of Priebe et al. [49] and Pasquariello et al. [46], the low frequency mode exhibits large velocity fluctuations along the separated shock, whereas contributions from the incident shock region are negligible. Secondly, significant perturbations concentrate around the separated shear layer above the separation bubble, especially close to the wall at x =-40 mm. Fluctuations are also observed inside the bubble and in the downstream region. However, the spatial structures for the type II modes are dominated by alternatively positive and negative fluctuations along the separated shear layer and induced Mach waves originating from the boundary layer edge. Compared to the type I mode, the separated shock is significantly wrinkled by the incoming fluctuations and the shear layer vortices, in agreement with the finding of Pasquariello et al. [46]. Fig. 25 shows two medium frequency (type II) modes, i.e. $f_{\mathrm{II}} = 0.1U_\infty/\delta$ and $f_{\mathrm{II}} = 0.2U_\infty/\delta$ for IN-10**.** As can be seen, these two modes exhibit qualitatively similar behavior to the type II modes of IN-0, suggesting that the expansion corner has little influence on the spatial character of the medium frequency unsteadiness in the interaction region. Such a similarity can be explained as follows: the medium frequency fluctuations are strongly associated with the passage of turbulent structures, whereas the low frequency unsteadiness is mainly driven by the instability of the downstream system including the separated shock, the separated shear layer and the separation bubble. As a result, the low frequency modes do not play a dynamically relevant role in the entire time history. Overall, the expansion effect on the incoming turbulent boundary layer is negligible, and the medium frequency modes play the leading role in the interaction region.

6. Conclusions

In the present study, direct numerical simulations are conducted for incident shock wave and supersonic turbulent boundary layer interactions near an expansion corner at $M_\infty = 2.9$ and $Re_\infty = 5581$, and the flow characteristics are thoroughly investigated for four different expansion angles, i.e. 0^0, 2^0, 5^0 and 10^0. The main objective is to analyze the expansion effect on the separation region, statistics of the post-shock turbulent boundary layer and the unsteadiness associated with the interaction region. The mean wall pressure and skin-friction coefficient distribution are compared against previous experimental and numerical results and a satisfactory agreement is achieved.

The coherent vortex structures in the interaction region are analyzed using the Q criterion. It is found that the vortex structures are significantly strengthened by the shock wave interaction, and a remarkable weakening of large-scale vortexes occurs in the outer layer of the reattachment boundary layer along the expansion corner. The results suggest that the expansion corner reduces the extent of the separation bubble, while preferentially suppresses the three-dimensionality at the reattachment point. It is found that the scaling analysis of the interaction length given by Souverein et al. [30] is not equally applicable for flow with expansion, thus a new scaling formula is proposed to quantify the expansion effect by adding an additional term into the trigonometrical correction factor.

As the expansion angle is increased, the mean velocity and Reynolds shear stress in the reattached turbulent boundary layer undergo a faster recovery to the equilibrium state. The turbulent kinetic energy is significantly decreased with a corresponding reduction of the production peak in the outer region, whereas an increase of the turbulence production is more pronounced in the near-wall region. The budget analysis demonstrates that the expansion has no essential influence on the budget balance, similar to the incoming turbulent boundary layer.

Spectral analysis of wall pressure fluctuations suggests that no evident low frequency unsteadiness is observed when the angle of the expansion corner is increased to 10^0, and the remaining unsteady motions are characterized by medium frequencies. Based on the dynamic mode decomposition, it is found that the low frequency modes are strongly associated with the separated shear layer and the separation bubble in the downstream region, whereas the medium frequency modes are related with flow structures originating from the incoming turbulent boundary layer.

Acknowledgments

This work was supported by NSFC Projects (Nos. 91852203, 11972356), the National Key Research and Development Program of China (2016YFA0401200), Science Challenge Project (TZ2016001), and Strategic Priority Research Program of Chinese Academy of Sciences (Grant no. XDA17030100). The authors thank National Supercomputer Center in Tianjin (NSCC-TJ), and National Supercomputer Center in Guangzhou (NSCC-GZ) for providing the computational time.

References

[1] Clemens NT, Narayanaswamy V. Low-frequency unsteadiness of shock wave/turbulent boundary layer interactions. Annu Rev Fluid Mech 2014;46:469–92.
[2] Gaitonde DV. Progress in shock wave/boundary layer interactions. Prog Aerosp Sci 2015;72:80–99.
[3] Narasimha R, Sreenivasan KR. Relaminarization of Fluid Flows. Adv Appl Mech 1979;19:221–309.
[4] Goldfeld MA, Nestoulia RV, Shiplyuk AN. Re-laminarization of a turbulent boundary layer with a Mach number M = 4. J Appl Mech Technol Phys 2002;43(1):76–82.

[5] Chew YT. Shock wave and boundary layer interaction in the presence of an expansion corner. Aeron Q 1979;30:506–27.
[6] Chung KM, Lu FK. Hypersonic turbulent expansion-corner flow with shock impingement. J Propul Power 1995;11(3):441–7.
[7] White ME, Ault DA. Expansion corner effects on hypersonic shock wave/turbulent boundary-layer interactions. J Propul Power 1996;12(6):1169–73.
[8] Sathianarayanan A, Verma SB. Experimental investigation of an incident shock-induced interaction near an expansion corner. J Spacecr Rockets 2017;54(3):769–73.
[9] Konopka M, Meinke M, Schroder W. Large-eddy simulation of relaminarization in supersonic flow; 2012. AIAA Paper No.2012-2978.
[10] Priebe S, Wu M, Martin MP. Direct numerical simulation of a reflected shock wave / turbulent boundary layer interaction. AIAA J 2009;47(5):1173–85.
[11] Bookey P, Wyckham C, Smits A. New experimental data of STBLI at DNS/LES accessible Reynolds numbers; 2005. AIAA paper No. 2005-309.
[12] Tong FL, Li XL, Duan YH, Yu CP. Direct numerical simulation of supersonic turbulent boundary layer subjected to a curved compression ramp. Phys Fluids 2017;29:125101.
[13] Li XL, Fu DX, Ma YW. Direct numerical simulation of hypersonic boundary layer transition over a blunt cone with a small angle of attack. Phys Fluids 2010;22:025105.
[14] Martin MP, Taylor EM, Wu M, Weirs VG. A bandwidth-optimized WENO scheme for the effective direct numerical simulation of compressible turbulence. J Comput Phys 2006;220:270.
[15] Pirozzoli S, Grasso F, Gatski TB. Direct numerical simulation and analysis of a spatially evolving supersonic turbulent boundary layer at M = 2.25. Phys Fluids 2004;16:530–45.
[16] Poinsot TJ, Lele SK. Boundary conditions for direct simulation of compressible viscous flow. J Comput Phys 1992;101:104–29.
[17] Wu M, Martin MP. Direct numerical simulation of supersonic turbulent boundary layer over a compression ramp. AIAA J 2007;45(4):879–89.
[18] Wu X, Moin P. Direct numerical simulation of turbulence in a nominally zero–pressure-gradient flat-plate boundary layer. J Fluid Mech 2009;630:5–41.
[19] Erm LP, Joubert PN. Low Reynolds number turbulent boundary layers. J Fluid Mech 1991;230:1–44.
[20] Pirozzoli S, Bernardini M. Direct numerical simulation database for impinging shock wave/turbulent boundary-layer interaction. AIAA J 2011;49(6):1307–12.
[21] Duan L, Choudhari MM, Wu M. Numerical study of acoustic radiation due to a supersonic turbulent boundary layer. J Fluid Mech 2014;746:165–92.
[22] Bernardini M, Pirozzoli S. Wall pressure fluctuations beneath supersonic turbulent boundary layers. Phys Fluids 2011;23:085102.
[23] Beresh SJ, Henfling JF, Spillers RW. Fluctuating wall pressure measured beneath a supersonic turbulent boundary layer. Phys Fluids 2011;23(7):075110.
[24] Farabee T, Casarella MJ. Spectral features of wall pressure fluctuations beneath turbulent boundary layers. Phys Fluids 1991;3:2410–20.
[25] Bull MK. Wall-pressure fluctuations associated with subsonic turbulent boundary layer flow. J Fluid Mech 1967;28:719–54.
[26] Jeong J, Hussain F. On the identification of a vortex. J Fluid Mech 1995;285:69–94.
[27] Pirozzoli S, Bernadini M, Grasso F. On the dynamical relevance of coherent vertical structures in turbulent boundary layers. J Fluid Mech 2010;648:325–49.
[28] Humble RA, Peltier SJ, Bowersox RDW. Visualization of the structural response of a hypersonic turbulent boundary layer to convex curvature. Phys Fluids 2012;24:106103.
[29] Simpson RL. Turbulent boundary layer separation. Annu Rev Fluid Mech 1989;21:205.
[30] Souverein LJ, Bakker PG, Dupont P. A scaling analysis for turbulent shock-wave/boundary-layer interactions. J Fluid Mech 2013;714:505–35.
[31] Jaunet V, Debieve JF, Dupont P. Length scales and time scales of a heated shock-wave/boundary-layer interaction. AIAA J 2014;52(11):2524–32.
[32] Quadros R, Bernardini M. Numerical investigation of transitional shock-wave/boundary-layer interaction in supersonic regime. AIAA J 2018;56(7):2712–24.
[33] Ringuette MJ, Bookey P, Wyckham C, Smits AJ. Experimental study of a Mach 3 compression-ramp interaction at Reδ=2400. AIAA J 2009;47(2):373–85.
[34] Ganapathisubramani B, Clemens NT, Dolling DS. Effects of upstream coherent structures on low-frequency motion of shock-induced turbulent separation; 2007. AIAA paper No. 2007-1141.
[35] Touber E, Sandham ND. Comparison of three large-eddy simulations of shock-induced turbulent separation bubbles. Shock Waves 2009;19(6):469–78.
[36] Polivanov P, Sidorenko A, Maslov A. Report on the measurement of shock reflection by Mach=2.0: Final Report," UFAST Deliverable 3.3.6. Novosibirsk, Russia: Khristianovich Inst. of Theoretical and Applied Mechanics (ITAM); 2009.
[37] Laurent H. Turbulence d'une Interaction Onde de Choc-Couche Limite sur Paroi Plane Adiabatique ou Chauffée Ph.D. Thesis. Marseille, France: Université d'Aix-Marseille II; 1996.
[38] Sun MB, Hu ZW, Sandham ND. Recovery of s supersonic turbulent boundary layer after an expansion corner. Phys Fluids 2017;29:076103.
[39] Wu M, Martin MP. Analysis of shock motion in shock wave and turbulent boundary layer interaction using direct numerical simulation data. J Fluid Mech 2008;594:71–83.
[40] Priebe S, Martin MP. Low-frequency unsteadiness in shock wave-turbulent boundary layer interaction. J Fluid Mech 2012;594:1–49.
[41] Grilli M, Schmid PJ, Hickel S, Adams NA. Analysis of unsteady behavior in shock wave turbulent boundary layer interaction. J Fluid Mech 2012;700:16–28.
[42] Nichols JW, Larsson J, Bernardini JM, Pirozzoli S. Stability and modal analysis of shock/boundary layer interactions. Theor Comput Fluid Dyn 2016;31(1):33–50.
[43] Erengil ME, Dolling DS. Unsteady wave structure near separation in a Mach 5 compression ramp interaction. AIAA J 1991;29(5):728–35.
[44] Dussauge JP, Dupont P, Debieve JF. Unsteadiness in shock wave boundary layer interactions with separation. Aerosp Sci Technol 2006;10:85–91.
[45] Morgan B, Duraisamy K, Nguyen N, Kawai S, Lele SK. Flow physics and RANS modeling of oblique shock/ turbulent boundary layer interaction. J Fluid Mech 2013;729:231–84.
[46] Pasquariello V, Hickel S, Adams NA. Unsteady effects of strong shock-wave/boundary-layer interaction at high Reynolds number. J Fluid Mech 2017;823:617–57.
[47] Schmid PJ. Dynamic mode decomposition of numerical and experimental data. J Fluid Mech 2010;656:5–28.
[48] Jovanovi MR, Schmid PJ, Nichols JW. Sparsity-promoting dynamic mode decomposition. Phys Fluids 2014;26:024103.
[49] Priebe S, Tu JH, Rowley CW, Martin MP. Low-frequency dynamics in a shock-induced separated flow. J Fluid Mech 2016;807:441–77.